The reuniens nucleus of the thalamus facilitates hippocampo-cortical dialogue during sleep

Diellor Basha[1,2], Amirmohammad Azarmehri[3], Eliane Proulx [1,#], Sylvain Chauvette[2], Maryam Ghorbani[3], Igor Timofeev[1,2,*]

[1]Département de psychiatrie et de neurosciences, Université Laval, Québec, QC, G1V 0A6, Canada
[2]CERVO Centre de recherche, Université Laval, Québec, QC, G1E 1T2, Canada
[3]Department of Electrical Engineering, Ferdowsi University of Mashhad, Mashhad, Iran

[#]Current address: CNS Diseases Research, Boehringer Ingelheim Pharma GmbH & Co. KG, Biberach an der Riß, Baden-Württemberg, Germany

*Lead contact and correspondence: igor.timofeev@fmed.ulaval.ca

Summary

Memory consolidation during sleep depends on the interregional coupling of slow waves, spindles, and sharp wave-ripples (SWRs), across the cortex, thalamus, and hippocampus. The reuniens nucleus of the thalamus, linking the medial prefrontal cortex (mPFC) and the hippocampus, may facilitate interregional coupling during sleep. To test this hypothesis we used intracellular, extracellular unit and local field potential recordings in anesthetized and head restrained non-anesthetized cats as well as computational modelling. Electrical stimulation of the reuniens evoked both antidromic and orthodromic intracellular mPFC responses, consistent with bidirectional functional connectivity between mPFC, reuniens and hippocampus in anesthetized state. The major finding obtained from behaving animals is that at least during NREM sleep hippocampo-reuniens-mPFC form a functional loop. SWRs facilitate the triggering of thalamic spindles, which later reach neocortex. In return, transition to mPFC

UP states increase the probability of hippocampal SWRs and later modulate spindle amplitude. During REM sleep hippocampal theta activity provides periodic locking of reuniens neuronal firing and strong crosscorrelation at LFP level, but the values of reuniens-mPFC crosscorrelation was relatively low and theta power at mPFC was low. The neural mass model of this network demonstrates that the strength of bidirectional hippocampo-thalamic connections determines the coupling of oscillations, suggesting a mechanistic link between synaptic weights and the propensity for interregional synchrony. Our results demonstrate the presence of functional connectivity in hippocampo-thalamo-cortical network, but the efficacy of this connectivity is modulated by behavioral state.

Impact Statement

The nucleus reuniens of the thalamus play a central role in synchronizing the mPFC-hippocampal network during sleep and integrates converging activity from hippocampal and mPFC oscillations.

Keywords

Nucleus reuniens, hippocampus, medial prefrontal cortex (mPFC), slow waves, sleep, spindles, sharp wave-ripples (SWRs), interregional synchrony, neural mass model, phase amplitude coupling

Introduction

Interactions between the hippocampus and the medial prefrontal cortex (mPFC) are essential for cognition. During sleep, hippocampal and cortical activity is continually synchronized by cardinal sleep oscillations such as slow waves (SWs, 0.1-4 Hz), thalamocortical spindles (10-15 Hz), and hippocampal sharp-wave ripples (SWRs, 100-300 Hz) (Isomura et al., 2006; Siapas and Wilson, 1998). These rhythms have well-known roles in neuronal plasticity (Chauvette et al., 2012; Diekelmann and Born, 2010) and in the consolidation of hippocampus-dependent memories (Maingret et al., 2016). In particular, the hierarchical coupling of slow waves, spindles and SWRs is thought to play a key role in memory consolidation (Diekelmann and Born, 2010). Consistent with this hypothesis, the temporal coupling of hippocampal and mPFC sleep oscillations results in a selective increase in the recall of hippocampus-dependent memory (Latchoumane et al., 2017; Maingret et al., 2016).

At present, the pathways that coordinate the long-range coupling of slow waves, spindles and SWRs across the prefronto-hippocampal network are not well characterized. Although the hippocampus extends projections to several prefrontal areas(Cavada et al., 1983; Goldman-Rakic et al., 1984; Irle and Markowitsch, 1982; Jay and Witter, 1991; Swanson, 1981), few regions of the prefrontal cortex reciprocate(Rajasethupathy et al., 2015). With respect to medial regions of the prefrontal cortex, no direct projections to the hippocampus have been identified(Beckstead, 1979; Goldman-Rakic et al., 1984; Reep et al., 1987; Room et al., 1985; Takagishi and Chiba, 1991).

67 The nucleus reuniens of the thalamus (reuniens) is bidirectionally connected to the
68 hippocampus and the mPFC (Herkenham, 1978; Vertes et al., 2007), making it an ideal hub for
69 coupling hippocampo-cortical interactions during sleep. Reuniens is part of the ventral group of
70 midline thalamic nuclei with widespread connections to cortical, thalamic, hypothalamic and
71 brainstem structures (Herkenham, 1978; McKenna and Vertes, 2004; Ohtake and Yamada,
72 1989; Robertson and Kaitz, 1981; Vertes et al., 2006). Consistent with its anatomical
73 connections to the hippocampus and the mPFC, reuniens plays a major role for memory
74 function(Ramanathan et al., 2018; Xu and Sudhof, 2013) and a growing body of evidence points
75 its critical role in processing hippocampus-dependent memory (Ramanathan and Maren, 2019;
76 Ramanathan et al., 2018). Although evidence for the functional significance of reuniens in
77 cognitive operations is strong, little is known about the nature of reuniens-prefrontal
78 interactions and their interplay with hippocampal events during sleep (Di Prisco and Vertes,
79 2006).

80 Considering the well-established link between sleep and memory consolidation (Diekelmann
81 and Born, 2010; Frankland and Bontempi, 2005; Timofeev and Chauvette, 2019), we
82 investigated the role of the reuniens in coupling hippocampo-cortical oscillations during non-
83 rapid eye movement (NREM) and REM sleep. Using in vivo intracellular recordings,
84 computational modelling, and spike/local field potential (LFP) recordings, we demonstrate that
85 reuniens is driven by hippocampal oscillations during sleep and that it elicits fast, consistent
86 synaptic responses in mPFC. Hippocampal and reuniens activity precedes the onset of mPFC
87 spindles, suggesting a hippocampo-thalamic trigger for spindle initiation. In turn, the phase of

mPFC slow waves determined the amplitude of reuniens spindles and of SWR timing, forming a functional feedback loop through the reuniens.

Results

Reuniens elicits fast, consistent synaptic responses in the mPFC

We obtained intracellular recordings of mPFC neurons in vivo (n=49 neurons) during targeted, electrical stimulation of the ventral hippocampus and reuniens from 16 anesthetized cats (Figure 1A-D). Stimulation of the hippocampus and reuniens elicited synaptic responses in 55% and 51% of recorded mPFC neurons, respectively. Hippocampal stimulation generated variable responses in the same neurons, consisting of complex sequences of either two excitatory postsynaptic potentials (EPSPs) followed by long-lasting hyperpolarization (Figure 1E, top, left), a depolarization-hyperpolarization sequence (Figure 1E, middle, left), or no response (Figure 1E, bottom, left). The polarity of early depolarizing responses elicited by hippocampal stimulation was dependent on membrane potential, reversing with progressive depolarization of the membrane at around -70 mV (Figure 1E, right), suggesting that the initial depolarization was an inhibitory postsynaptic potential (IPSP).

Reuniens stimulation elicited consistent EPSPs followed by long-lasting hyperpolarization (Figure 1C, bottom) at earlier latencies than hippocampal stimulation (6.05±3.6 ms for reuniens and 9.95±4.6 ms and hippocampal stimulation, respectively, t-test, $p<0.01$, Figure 1G). EPSPs elicited by reuniens stimulation had faster rising slopes compared to hippocampal stimulation (0.56±0.27 V/s for reuniens and 1.9±0.9 V/s for hippocampal stimulation, t-test, $p<0.01$) but

108 were of lower amplitude (3.1±2.0 mV for reuniens and 8.4±4.1 mV for hippocampal stimulation,
109 t-test, $p<0.01$). We observed no significant difference in the duration of the late,
110 hyperpolarizing component in response to reuniens and hippocampal stimulations.

111 Reuniens stimulation elicited action potentials that were either orthodromic (85%), antidromic
112 (10%) or both (5%), evidenced by jitter in the latency of orthodromic action potentials and
113 consistent latency of antidromic action potentials (Figure 1F). Antidromic responses to reuniens
114 stimulation, confirmed by collision tests, were recorded in cells located 6050-6600 µm ventral
115 to the dorsal aspect of the cortical surface. The mean latency of antidromic spikes was 2.9±0.25
116 ms (mean ± SD).

117 To characterize the prefrontal topography of reuniens and hippocampal receptive fields, we
118 descended a 4-shank microelectrode array into the mPFC in 1 mm steps and recorded evoked
119 field potentials in response to reuniens and hippocampal stimulation (Figure 1H). Reuniens
120 stimulation evoked field postsynaptic potential in a wider prefrontal territory compared to
121 hippocampal stimulation which was restricted to the ventroposterior part of the mPFC. In some
122 locations of mPFC, early responses to reuniens stimulation (Figure 1 H, I) corresponded to
123 criteria of field potential antidromic responses(Chang, 1953). Areas in the prefrontal cortex that
124 responded to hippocampal stimulation overlapped with areas exhibiting antidromic responses
125 to reuniens stimulation (Figure 1 I, shadowed area) which corresponds to area 32 of the
126 prelimbic cortex. In the following experiments, we targeted this region of the mPFC.

Reuniens and ventral hippocampal activity precede the onset of mPFC spindles

Sleep enhances communication in the hippocampo-cortical pathway by promoting interregional synchrony through highly rhythmic events such as slow waves and spindles. To investigate the role of the reuniens in mediating synchrony in the mPFC-hippocampal network, we performed LFP recordings of the mPFC and ventral hippocampus, as well as targeted spike/LFP recordings of the reuniens during natural sleep from 4 cats (Figure 2A, Figure 2 – figure supplement 1). Recordings were segmented into wake, NREM and REM epochs, based on mPFC delta power, mPFC signal amplitude, and nuchal muscle activity (Figure 2 B-D). During NREM sleep, LFP recordings and corresponding wavelet transforms of the signal suggested correlated activity among mPFC slow waves, spindles, hippocampal SWRs, and reuniens multi-unit activity (Figure 2E). We observed co-occurring reuniens and mPFC spindles (Figure 2F), characterized by significantly earlier onset of reuniens spindles relative to the onset of mPFC spindles (median = -0.083 s, n=49 sessions, Figure 2G).

NREM sleep analysis of reuniens single-unit activity relative to the phase of mPFC and reuniens spindle cycles revealed significant phase-locking of reuniens single-units to mPFC spindle cycles (n= 24/49 single-units, mean ± SD = -80.87 ± 41.64°, $p = 2.942 \times 10^{-7}$, Rayleigh test, Figure 2H) and reuniens spindle cycles (n= 29/49 single-units, mean ± SD = -118.25 ± 47.72°, $p = 1.047 \times 10^{-6}$, Rayleigh test Figure 2I). The mean phase preference of reuniens single-units was advanced for reuniens spindle cycles relative to mPFC spindle cycles. For pairs of co-occurring reuniens and mPFC spindles, spindle amplitudes were significantly correlated (r=0.54 using mPFC spindle as

reference, $p = 3.22 \times 10^{-27}$, Figure 2J, and $r=0.47$, $p = 8.61 \times 10^{-25}$ when using Reuniens spindle as reference, Figure 2K).

Lastly, we investigated during NREM sleep the change in hippocampal and reuniens signal power during mPFC spindles relative to baseline, which demonstrated increased hippocampal ripple power and increased reuniens spindle power preceding the onset of spindles in the mPFC (Figure 2L, top). The histogram of SWR incidence in the same time window, referenced to the onset of mPFC spindles, indicated increased SWR incidence prior to the onset of mPFC spindles (Figure 2L, middle). Reuniens multi-unit activity increased prior to the onset of mPFC spindles (Figure 2L, bottom).

mPFC slow waves - spindle phase amplitude coupling in the reuniens-mPFC network

To examine the modulation of reuniens and hippocampal activity by mPFC slow waves, we analyzed the relationship between the phase of mPFC slow waves with respect to spindles and SWRs during NREM sleep. Figure 3A shows a representative example of a coupled slow wave-spindle event from simultaneous recordings of the mPFC and reuniens. We analyzed the average time-frequency representation of mPFC amplitudes locked to the peak of the mPFC slow wave (Figure 3B), as well as the average time-frequency representations of reuniens amplitudes, locked to the peak of the same mPFC slow waves (Figure 3C), which showed significant modulation of spindle amplitudes by the phase of the mPFC slow wave.

168 The strength of slow wave-spindle coupling, estimated by the absolute value of the
169 synchronization index (SI) was higher for mPFC slow wave-reuniens spindle coupling compared
170 to mPFC slow wave-mPFC spindle coupling (median ± mean absolute deviation [MAD], SI
171 strength = 0.18 ± 0.09 and 0.24 ± 0.11 for mPFC and reuniens spindles, respectively, $p = 2.126 \times$
172 10^{-17}, Wilcoxon signed rank test, Figure 3 D). A comparison of slow wave-spindle coupling
173 strength between mPFC-mPFC pairs and mPFC-reuniens pairs is shown in Figure 3E. The
174 amplitude of reuniens spindles increased at earlier phases of the mPFC slow wave compared to
175 the amplitude of mPFC spindles, which increased at later phases of the mPFC slow wave (Figure
176 3B,C,F). This finding suggests that mPFC can trigger reuniens spindles, but spindles recorded in
177 mPFC are not necessarily imposed by reuniens spindles.

178 Next, we examined the relative delays in the timing of mPFC and reuniens slow waves during
179 NREM sleep. Figure 3G shows a representative example of an overlapping mPFC and reuniens
180 slow wave, with circles indicating slow wave peaks. Single session data in Figure 3H
181 demonstrates the delay between reuniens and mPFC slow waves, showing significant lag in the
182 time of reuniens slow waves relative to mPFC slow waves (median ± MAD = 0.126 ± 0.043 s, $p =$
183 3.66×10^{-15}, $n = 82$, Wilcoxon signed rank test). The distribution of median delay times for all
184 recording sessions between each reuniens-mPFC slow wave pair are shown in Figure 3I.

185 Lastly, we analyzed the phase-locking of ventral hippocampal SWRs to mPFC slow waves. Figure
186 3J shows a representative example of a coupled slow wave-SWR event. The distribution of slow
187 wave phases at the time of SWRs was non-uniform, indicating significant phase-locking of SWRs
188 to mPFC slow waves at a mean phase of 162.7± 29.37° ($p = 5.02 \times 10^{-6}$, Rayleigh test, Figure

189 3K). We found no significant phase-locking of SWRs to spindle cycles in the majority of
190 recording sessions (n=3/51 with significant phase for mPFC spindle-SWR and n=10/51 sessions
191 with significant phase for reuniens spindle-SWR coupling, Figure 3 – figure supplement 1 and
192 Table 1).

193 Hippocampal oscillations modulate reuniens activity

194 Considering the comodulation of reuniens and hippocampal activity prior to mPFC spindles, we
195 asked whether hippocampal oscillations directly influence firing activity in the reuniens. A
196 representative example of LFP recordings of the ventral hippocampus, mPFC, and reuniens
197 during REM sleep is shown in Figure 4A. The wavelet spectrogram of the hippocampal trace
198 demonstrates prominent theta-band activity during REM with periodic locking of reuniens
199 multi-unit activity to hippocampal theta cycles (Figure 4B). Analysis of reuniens firing around
200 the peak of hippocampal theta cycles, shows significant phase-locking of reuniens single-unit
201 activity to the theta rhythm during REM (Figure 4C-F).

202 Power spectra of mPFC, reuniens, and hippocampal signals during REM are characterized by
203 prominent peaks in the theta range, with coherence between mPFC-hippocampus, reuniens-
204 hippocampus, and mPFC-reuniens recording pairs in the theta range during REM (Figure 4 G, H).
205 mPFC-reuniens recordings were further comodulated by a slow, irregular potential observed in
206 Figure 4A and in the broad low frequency peak (Figure 4H, bottom). Cross-correlations and
207 relative time lags of reuniens-hippocampus and mPFC-hippocampus recording pairs during REM
208 are illustrated in Figure 4I. mPFC signals lagged hippocampal signals by a longer delay than
209 reuniens signals lagged hippocampus (mean lag ± SD = 87.8 ± 55.5 ms and 109.1 ± 41.52 for

210 reuniens and mPFC, respectively, n=20 sessions, p=0.002, t-test ,Figure 4J, top) and peak cross-
211 correlation coefficients were significantly higher for reuniens-hippocampus recording pairs than
212 for reuniens-mPFC (mean peak value ± SD = 0.44 ± 0.13 and 0.22 ± 0.07 for reuniens and mPFC
213 respectively=20 sessions, t-test, $p<10^{-20}$, Figure 4J, bottom).

214 Next, we analyzed reuniens firing activity during SWRs in NREM. Figure 4K shows representative
215 LFP recordings of the hippocampus and reuniens multiunit activity during SWR events in NREM
216 sleep. In 20.4 % of reuniens single-units (10/49), firing rate increased significantly following the
217 onset of SWRs in the hippocampus, compared to shuffled events in the same period (Figure 4L,
218 150 ms post-SWR onset). Firing rates decreased significantly in 32.6% (16/49) of single-units
219 following SWR onset. The average thalamic LFP around the onset of the SWR was characterized
220 by a negative, 250 μV deflection coincident with increased reuniens firing.

221 Hippocampal-thalamocortical model

222 To explore the parameters that control interregional synchrony during NREM sleep, we
223 constructed a neural mass firing rate model consisting of two cortical networks (N 1 & 2),
224 representing mPFC layers 5 and 6, respectively, and two hippocampal (CA1-CA3) and three
225 thalamic networks (TRN, MD, and Reu, Figure 5A). Sharp waves and slow waves are
226 spontaneously generated in the isolated CA3 and cortical networks respectively as a result of
227 adaptation and excitatory-to-excitatory recurrent connections. SWRs are reproduced in the CA1
228 network during the active phase of the sharp wave due to recurrent connections between the
229 CA1 excitatory and inhibitory neurons with the firing rates sharply dependent on the
230 membrane potential in this firing rate model (Azimi et al., 2021). The oscillations in the range of

spindle frequency are spontaneously generated in the bursting, recurrently connected MD-TRN network. The beginning and end of the spindles are controlled by cortical inputs in the thalamocortical model with long-range bidirectional projections between cortical and thalamic networks. In the full hippocampo-cortico-thalamic model, the CA1 is directly connected to the cortical network while reuniens, which is bidirectionally connected to both CA1 and cortical networks, mediates the cortical to CA1 influence. With large enough strength of multi-regional projections, the model can spontaneously reproduce the experimentally observed coupling between the slow waves, spindles, and SWRs (Figure 5B). We found that reuniens slow waves occur significantly later than cortical slow waves (median ± MAD = 0.113 ± 0.019 s, $p < 10^{-20}$, Wilcoxon signed rank test, Figure 5C). In contrast, thalamic spindles occur significantly earlier than cortical spindles (median ± MAD = -0.102 ± 0.387 s, $p = 1.30 \times 10^{-7}$, Wilcoxon signed rank test, Figure 5D).

Figure 5E shows the average of cortical slow wave trough-locked time-frequency representations of the membrane potential of mPFC excitatory neurons and reuniens neurons. The slow wave-spindle coupling angles are nonuniformly distributed for both cortical and reuniens spindles indicating strong coupling with slow waves (mean ± SD = 148.7 ± 23.9°, $p < 10^{-20}$ and 27.4 ± 20.4°, $p < 10^{-20}$, for mPFC and reuniens respectively, Rayleigh test). In quantitative match to the experimental data, reuniens spindles occur mainly around the slow wave peak (active phase) while cortical spindles mainly occur around the slow wave trough. The slow wave-spindle coupling strength is also higher for reuniens than cortical spindles (median ± MAD SI strength = 0.58 ± 0.11 and 0.66 ± 0.15 for mPFC and reuniens, respectively, $p = 8.45 \times 10^{-9}$, Wilcoxon signed rank test, Figure 5F). Slow waves in the thalamocortical network are also

accompanied by large negative deflections and a subsequent peak in CA1 network (Figure 5G). Phase locking analysis revealed that, consistent with the experimental data, SWRs are phase-locked to slow waves, occurring mainly before slow wave peaks (active phase, mean ± SD = -24.97 ± 62.01°, $p < 10^{-20}$, Rayleigh test, Figure 5H). The bidirectional projections between reuniens and CA1 coordinate the communication between these two networks so that the membrane potential of the reuniens neurons increases after SWRs (Figure 5I). Reuniens spindles were also preceded by an increase in the SWR rate (Figure 5J, the peak SWR rate occurs 0.32 s before the spindle onset).

Bidirectional projections between the reuniens and CA1 control multiregional interactions

To investigate how bidirectional projections between the reuniens and CA1 control multiregional interactions in the model, we explored hippocampal-thalamocortical coupling during sleep rhythms as a function of the strength of bidirectional projections between reuniens and CA1. The correlation between reuniens and CA1 membrane potentials during SWRs increased by increasing the strength of CA1 to reuniens projections (Figure 6A). In addition, the SWR activity before spindle onset is an increasing function of bidirectional projections between CA1 and reuniens (Figure 6B). Next, we studied the effect of the strength of reuniens-CA1 bidirectional projections on CA1 activity during cortical slow waves. The peak-to-trough magnitude of CA1 deflections around the cortical slow wave also increases by increasing the reuniens-CA1 bidirectional projections (Figure 6C). The slow wave mean phase at the time of SWR occurrence decreased by increasing the strength of the bidirectional

projections between reuniens and CA1 so that SWRs mostly occur before and after slow wave peak for strong and weak projections, respectively (Figure 6D). These results suggest that for strong reuniens-CA1 projection, the depolarizing input from reuniens during down-to-up transition is large enough to induce the SWRs in CA1 before the slow wave peak. Further, slow wave phases at the time of SWR occurrence are more nonuniformly distributed for stronger CA1-reuniens projection, indicating stronger phase locking of SWRs to slow waves.

Discussion

This study examined the functional relationship between mPFC, reuniens, and hippocampal activity in cats using electrophysiological and computational approaches. We found that reuniens activity during natural sleep was strongly modulated by hippocampal oscillations, and that reuniens-mPFC spindles were preceded by increased probability of hippocampal SWRs and ripple power. Electrical stimulation of reuniens generated orthodromic and antidromic spiking in mPFC neurons, indicating bidirectional thalamocortical circuitry between the mPFC and reuniens. Slow waves in reuniens lagged prefrontal slow waves but spindles in reuniens led prefrontal spindles, suggesting a bidirectional, oscillation-dependent dialogue between reuniens and the mPFC. Spindle amplitude and SWR occurrence was modulated by the phase of the prefrontal slow oscillation, consistent with the idea that prefrontal slow waves control the timing of thalamic and hippocampal events. Overall, the study provides physiological confirmation to the hypothesis that reuniens is a core mediator in hippocampo-cortical dialogue.

294 **Monosynaptic and polysynaptic hippocampal to mPFC connections.**

295 Hippocampal influence on the activity of prefrontal neurons is a central mechanism in sleep-
296 dependent memory consolidation (Bontempi et al., 1999; Siapas et al., 2005; Wilson and
297 McNaughton, 1994). Previous research has shown that response latency in the hippocampo-
298 prefrontal pathway exhibits substantial variability (Degenetais et al., 2003), indicating the
299 involvement of both monosynaptic and polysynaptic mechanisms in prefrontal response to
300 hippocampal input. Our findings support this notion, as we observed inconsistent mPFC
301 responses to hippocampal stimulation, occurring later than those elicited by reuniens
302 stimulation. Notably, the same cell in mPFC could respond or not respond to hippocampal
303 stimuli (Figure 1 C, E) while LFP responses were less variable. This was possibly due to inhibitory
304 mechanisms such as shunting/feedforward inhibition or cholinergic, monoaminergic, or
305 thalamic gating mechanisms (Floresco and Grace, 2003; Gigg et al., 1994; Gioanni et al., 1999;
306 Mansvelder et al., 2009; Robbins, 2005; Williams and Goldman-Rakic, 1995).

307 **Reuniens to mPFC pathway induces more reliable responses than**
308 **hippocampus to mPFC pathway.**

309 While the functional impact of the hippocampo-prefrontal pathway has been extensively
310 studied, there are fewer studies on the effects of reuniens on the prefrontal cortex (Di Prisco
311 and Vertes, 2006). In our study, half of recorded prefrontal cells responded to reuniens
312 stimulation, with a mean response latency of 6 ms and with antidromic spikes with a latency of
313 approximately 3 ms, pointing to bidirectional functional connectivity between the two
314 structures. Similarly, electrical stimulation of the reuniens/rhomboid nucleus in rats (Di Prisco

315 and Vertes, 2006) elicits prominent evoked potentials in prefrontal cortices that have putatively
316 monosynaptic latencies of 4.5 ms. We found that mPFC responses to reuniens stimulation were
317 qualitatively different from responses elicited by hippocampal stimulation, with significant
318 differences in latency, amplitude, slope of EPSPs, and duration of hyperpolarization. Reuniens-
319 evoked responses occurred earlier and were more consistent than hippocampal-evoked
320 responses, suggesting higher response fidelity in the reuniens-prefrontal pathway than in the
321 hippocampo-cortical pathway. Both pyramidal cells and inhibitory neurons mediate the
322 hippocampo-prefrontal response, with the early component thought to be primarily mediated
323 by AMPA receptors (Degenetais et al., 2003; Jay et al., 1992) and the early hyperpolarization
324 was likely mediated by $GABA_A$ and the late component by either $GABA_B$ conductances
325 (Degenetais et al., 2003) or it was mediated by disfacilitation(Contreras et al., 1996; Fuentealba
326 et al., 2004). mPFC interneurons also respond to hippocampal stimulation, with a shorter
327 response latency than pyramidal cells, suggesting that the hippocampus can exert feedforward
328 inhibition in the medial prefrontal cortex (Tierney et al., 2004), which could explain the polarity
329 reversal of mPFC neurons response around -70 mV to hippocampal stimulation (Figure 1 E).
330 AMPA excitation and GABA inhibition may also mediate the primary depolarizing and secondary
331 hyperpolarizing responses to reuniens stimulation in medial prefrontal cells (Figure 1 C, F)
332 similar to previously demonstrated mediodorsal-prefrontal pathway (Gigg et al., 1992). Similar
333 to hippocampal afferents to the mPFC, the reuniens nucleus sends glutamatergic afferents to
334 the prefrontal cortex (Hur and Zaborszky, 2005; Pirot et al., 1995) enabling influence on the
335 prefrontal neuronal activity.

A potential role of Reuniens to synchronize mPFC and hippocampal activity

Reuniens is believed to play a critical role in connecting the prefrontal cortex and hippocampus due to its bidirectional connections with both structures (Di Prisco and Vertes, 2006). The prefrontal cortex and hippocampus are both essential for memory processing (Bontempi et al., 1999), and previous research indicates the reuniens may synchronize the activity of these two structures (Ferraris et al., 2018). Demonstrations that the nucleus reuniens exerts excitatory actions at the CA1 (Bertram and Zhang, 1999; Dolleman-Van der Weel et al., 1997) and also at the prefrontal cortex (Di Prisco and Vertes, 2006) (intracellularly confirmed and described in our study) provides supporting evidence for this claim that nucleus Reuniens might synchronize the activity of ventral hippocampus and mPFC. We also found that hippocampal stimulation evoked strong responses in cortical areas coincident with the recording site of antidromic responses to reuniens stimulation (Figure 1). These results support the idea that the reuniens nucleus, ventral hippocampus, and prefrontal cortex form a functional loop, with the prefrontal cortex acting as a mediator of the hippocampo-prefronto-thalamic relay.

In NREM sleep, the coupling of hippocampal SWRs to cortical slow waves and thalamocortical spindles is thought to be the main network mechanisms by which the brain promotes the consolidation of short-term memory into long-term storage (Frankland and Bontempi, 2005; Maingret et al., 2016). However, the mechanism that governs the emergence of this interregional synchrony remains unclear. We found that reuniens single-unit activity exhibited sporadic locking to ventral hippocampal theta cycles (during REM sleep) and was strongly

357 modulated by ventral hippocampal SWRs. These results are congruent with findings in MD
358 thalamic nucleus showing that although overall CA1 ripples suppress MD firing, at the onset of
359 spindles, the MD firing triggered by ripples was increased (Yang et al., 2019). The firing pause in
360 reuniens neurons during SWR and the presence of spike-bursts after SWR suggests that the
361 spike burst is a rebound from previous hyperpolarization (Jahnsen and Llinás, 1984). This
362 suggests that SWR drive some inhibitory cells that hyperpolarize at least MD and reuniens. If
363 hyperpolarization is strong enough, like during slow wave, it triggers rebound spike bursts.
364 Considering the strong influence of reuniens on prefrontal targets, the hippocampal modulation
365 of reuniens activity points to a thalamic pathway for the coupling of sleep rhythms. Although
366 the minimal requirement to generate spindles is the reticular thalamic nucleus (TRN) (Bazhenov
367 et al., 1999; Steriade et al., 1987) , our finding of increased SWR probability and ripple power
368 prior to the onset of thalamocortical spindles suggest that hippocampal drive through reuniens
369 may initiate the thalamocortical cascade of events that leads to spindles.

370 Does Reuniens generate spindles?

371 In first-order nuclei of the thalamus, cortical firing can trigger spindles by exciting
372 hyperpolarized neurons of the TRN, eliciting high-frequency spike bursts(Contreras and
373 Steriade, 1996). In turn, TRN bursts can drive IPSPs in thalamocortical neurons, eliciting
374 rebound low-threshold calcium spikes (Bazhenov et al., 1999) and developing the spindle
375 primarily through recurrent inhibitory-excitatory interactions between the TRN and
376 thalamocortical neurons(Contreras and Steriade, 1996). Cortical firing also contributes to
377 spindle synchronization and the maintenance of the spindle through its influence on the TRN

378 (Bonjean et al., 2011). Thus, cortical activation after the down state can initiate thalamocortical
379 spindling and lock the timing of spindles to the phase of the slow oscillation. However, less is
380 known about spindle generation in higher-order thalamic nuclei, especially in thalamic nuclei
381 with limbic circuitry such as reuniens. The circuitry is in place for spindle generation in the
382 reuniens nucleus: The reuniens is connected bidirectionally with the prefrontal cortex
383 (Herkenham, 1978; Vertes et al., 2007); layer 6 of the infralimbic cortex projects to the
384 anteromedial TRN (Cornwall et al., 1990), a region that projects to the reuniens nucleus (Çavdar
385 et al., 2008; Kolmac and Mitrofanis, 1997). Our results revealed that reuniens neuronal firing is
386 modulated by spindles, whether spindles were recorded by LFP electrodes located in the mPFC
387 cortex or in the reuniens nucleus (Figure 2). While reuniens nucleus neurons can generate low-
388 threshold calcium spike, they do not display hyperpolarization-activated current(Walsh et al.,
389 2017), likely limiting their ability to generate and maintain spindles. Of note, without MD in our
390 computational model, no spindles were generated (data not shown). In general, although first
391 order thalamocortical cells display inhibitory, spindle-like activities during cortical active state,
392 higher order thalamocortical cells show persistent depolarizing states, excluding their
393 possibility to generate spindle-related rebound spike bursts(Groh et al., 2014; Sheroziya and
394 Timofeev, 2014). The bidirectional connections of the reuniens to neocortical and archicortical
395 structures make it difficult to discern the possible triggering event that initiates the spindle in
396 this nucleus. We found that hippocampal SWRs trigger thalamic rebound burst firing and
397 precede the onset of reuniens and mPFC spindles, which points to SWRs as one of candidate
398 events for spindle initiation. In this regard, the strong excitatory drive emerging form the
399 hippocampus during SWRs may represent an ontogenetically different mechanism for the

400 initiation of spindles in the limbic circuitry. However, the generation and maintenance of
401 spindle cycles depend on burst firing from inhibitory structures such as the TRN. To date, it is
402 not yet clear whether the hippocampus influences inhibitory thalamic structures such as the
403 TRN or the zona incerta, although projections from subiculum to the rostral TRN were
404 previously described(Cavdar et al., 2008). We propose that hippocampal SWRs can initiate a
405 cascade of thalamocortical events, beginning with the excitation of reuniens, which in turn
406 excites the mPFC. This mPFC excitation leads to spindle activity generated through cortico-
407 thalamic feedback from the mPFC to other thalamic nuclei, such as the MD nucleus.

408 Our computational model recaptures our experimental findings.

409 Our computational model demonstrates the presence of cross-regional interactions
410 between the prefrontal cortex and its thalamic partners. The model confirmed that thalamic
411 slow waves occur significantly later than cortical slow waves, whereas thalamic spindles occur
412 significantly earlier than cortical spindles, recapturing our experimental findings and pointing to
413 the cortical origin of slow-wave activity and thalamic origin of spindles. The model predicts that,
414 while CA1 to reuniens connection strength plays a critical role in the modulation of reuniens
415 activity by SWRs, bidirectional connections between reuniens and CA1 are critical for SWR-
416 dependent triggering of spindles. Similarly, bidirectional reuniens and CA1 connections are
417 important for transmitting cortical slow wave activity to the CA1 region. With strong
418 bidirectional connections, the SWR occurred primarily before the slow wave active phase peak
419 and with weak connections, the SWR tended to occur after this peak. Given our experimental

findings (Figure 3, J-K) the model suggests that the effectiveness of bidirectional connections between reuniens and CA1 is particularly strong during NREM in cat.

Conclusion. Overall, in addition to well-known anatomical connectivity in CA1, reuniens, mPFC network, our results demonstrate the presence of functional connectivity in this network. However, the efficacy of this functional connectivity is modulated by behavioral state. Such flexibility can be explained by neuromodulation of intrinsic neuronal currents, synaptic strength and synaptic dynamic (Nadim and Bucher, 2014)

Materials and Methods

Experimental model and subject details

Experiments were carried out in accordance with the guidelines of the Canadian Council on Animal Care and were approved by the Committee for Animal Care of Université Laval and are consistent with ARRIVE guidelines. In 20 adult cats (16 anesthetized [acute, results in figure 1] during recording sessions and 4 chronically implanted, not anesthetized [chronic, results in figures 2, 3, 4] during recording sessions), aged 1-1.5 years, electrophysiological recordings were obtained from the mPFC, midline thalamus, hippocampus and/or various cortical areas including somatosensory, motor, auditory, associative, and visual cortex. Prefrontal intracellular recordings (n=15) and LFP-array recordings (n=9) were obtained from anesthetized animals and spike/local field potential (n=4) recordings were obtained from non-anesthetized animals during sleep and wake cycles.

Surgeries

Anesthetized Animals

For acute intracellular recordings, cats were anesthetized with a mixture of ketamine and xylazine (10-15 and 2-3 mg/kg i.m., respectively) and maintained in anesthetic state during the experiment by supplemental doses of ketamine (5 mg/kg). Body temperature was maintained at 37°C via a feedback-controlled heating pad and the heart rate was continuously monitored (90-110 bpm). All pressure points and incision sites were infiltrated with lidocaine (0.5%). Animals were paralyzed with gallamine triethiodide and artificially ventilated to an end-tidal CO_2 concentration of 3.5-3.8%. Recording stability was maintained by cannulation of the cisterna magna, bilateral pneumothorax, hip suspension, and by sealing craniotomies with agar solution (4% in 0.9% saline).

Non-anesthetized animals

For chronic spike/LFP recordings, cats were implanted with indwelling electrodes and a head-restraint system according to surgical procedures described previously in Timofeev et al. (2001) and Chauvette et al. (2011). Briefly, cats were pre-anesthetized with an intramuscular injection of ketamine (3 mg/kg), buprenorphine (0.02 mg/kg), and dexmedetomidine (5 µg/kg). The incision site was shaved, and the cats were intubated for gaseous anesthesia. Lidocaine (0.5%) and bupivacaine (0.25%) was injected at the site of the incision and in all pressure points where the head contacted the stereotaxic frame. Four stainless-steel electrodes were implanted under stereotaxic guidance in the mPFC (*from the interaural line: AP 23 to 24 mm, ML 1 mm, DV 5 mm, ϑ=10°*) according to the Reinoso-Suarez stereotaxic atlas of the cat brain (Reinoso-Suárez, 1961). Additionally, single stainless-steel electrodes were implanted in deep cortical layers (1.2

461 mm from cortical surface) in the ipsi- or contralateral hemisphere in the marginal gyrus [visual
462 cortex (areas 17 and 18)], suprasylvian gyrus [associative cortex (areas 5, 7, and 21)],
463 ectosylvian gyrus [auditory cortex (areas 22 and 50)], postcruciate gyrus [somatosensory cortex
464 (area 3)], precruciate gyrus [motor cortex (areas 4 and 6)]. Tetrodes, constructed out of four
465 twisted microwires (platinum-iridium, 12.5 µm, gold-plated to 190-210 kΩ), were implanted
466 into the midline thalamus (*from the interaural line: AP 11.5, ML 0.5, DV 1.5, ϑ=10°*) and into the
467 CA1 region of the hippocampus (*from the interaural line: AP 7, ML 10.5, DV -3.5, ϑ=10°*).

468 For electro-oculography (EOG), a silver electrode was implanted through the orbital bone and
469 for electromyography (EMG), two teflon-insulated stainless-steel electrodes were implanted
470 into the neck muscle. All recordings were referenced to a silver electrode fixed to the skull
471 above the cerebellum. To allow for subsequent head-restrained recordings, head-fixation
472 holders were also attached and encased into the dental cement. Throughout the surgery, the
473 body temperature was maintained at 37°C using a water-circulating thermo-regulated blanket.
474 Heartbeat, oxygen saturation and blood pressure were continuously monitored using a pulse
475 oximeter (Rad-8; MatVet), and the level of anesthesia was adjusted to maintain a heartbeat at
476 130-150 per minute. Lactate Ringer's solution was given intravenously (5 ml/ kg/h, i.v.) during
477 the surgery. After the surgery, cats received meloxicam (0.05 mg/kg) once a day for 3 days.

478 Electrophysiological recordings

479 *Acute recordings in anesthetized animals*

480 Intracellular recordings of the mPFC were obtained in vivo using glass micropipettes pulled on a
481 vertical puller (Narishige PP-830, Tokyo, Japan) from borosilicate capillary tubes (WPI; P-97,

482 Sutter Instrument) and filled with 3 M potassium acetate (DC resistances of 30- 60 MΩ). The
483 prefrontal region around the cruciate gyrus was targeted according to the stereotaxic cat atlas
484 of Reinoso-Suárez (1961) (*from the interaural line: AP 23 to 24 mm, ML 1 mm, DV 5-14.5 mm)*.
485 The micropipette was advanced dorsoventrally until a cell was penetrated, confirmed *in situ* by
486 electrophysiological observations and classification. A high-impedance amplifier (Neurodata IR-
487 283 amplifiers; Cygnus Technology) with active bridge circuitry was used to record the
488 membrane potential (sampled at 20 kHz) and to inject current into neurons.

489 Stimuli (0.2 ms, 0.3-1.5 mA) were delivered in single pulses at 1 Hz through bipolar (coaxial)
490 electrodes implanted in the ventral midline thalamus (*from the interaural line: AP 12, ML 0.0,*
491 *DV 1.0*) and hippocampus (*from the interaural line: AP 7.2, ML 10.5, DV -4.5)*. Bandpassed (0.1
492 Hz-10 kHz) field potentials were recorded through the same bipolar electrodes at 20 kHz
493 sampling.

494 To study the topography of prefrontal responses to thalamic and/or hippocampal stimulation,
495 an array of 4 tungsten microelectrodes (9-12 MΩ, 1 mm apart in the antero-posterior axis) was
496 positioned in the mPFC in 9 animals (ML 1.0, AP 26-23). The array was positioned close to the
497 midline in the pericruciate gyrus sigmoidus and advanced ventrally in 1 mm steps. At each step,
498 thalamic or hippocampal stimuli (0.2 ms, 0.3-1.5 mA) were delivered at 1 Hz or in 5-pulse trains
499 every 2 seconds at 5Hz, 10Hz, 20 Hz and 100 Hz through bipolar (coaxial) electrodes implanted
500 in the ventral midline thalamus (*from the interaural line: AP 12, ML 0.0, DV 1.0*) and
501 hippocampal formation (*from the interaural line: AP 7.2, ML 10.5, DV -4.5)*. Antidromic events
502 were detected according to methods described previously in Lipski (1981).

To label stimulation sites, electrolytic lesions were made through thalamic and hippocampal electrodes via 0.75 mA, 1 s current pulses, delivered every 3 s for 5 minutes.

Chronic recordings in non-anesthetized animals

For non-anesthetized cats, a post-operative recovery time of 1 week was maintained prior to the first recording session. Cats were trained over 2-3 days to remain in head-restrained position for 2– 4 h and cycle through periods of quiet wakefulness, NREM, and REM sleep. Recordings were obtained over two weeks following the post-operative recovery period. All recordings were conducted within a Faraday chamber using AM 3000 amplifiers (A-M Systems), bandpassed 0.1 Hz to 10 kHz with a 1k gain. All signals were sampled at 20 kHz and digitized with PowerLab (ADInstruments - Data Acquisition Systems for Life Science, RRID:SCR_001620).

Histology

Location of all electrodes was verified on histological sections from each animal. At the conclusion of experiments, animals were deeply anesthetized and perfused intracardially with 4°C saline (0.9%) followed by 4% paraformaldehyde (PFA) in 0.1 M phosphate buffer in saline (PBS). Brains were extracted and cryoprotected by immersion in several sucrose-PFA solutions of increasing sucrose concentration (10, 20 and 30% sucrose in PFA over 1 week). Brains were then sectioned in a freezing microtome (80 or 100 µm thickness), mounted on gelatinized glass slides, dried, and subsequently labelled with DAPI (300 nM, Invitrogen D3571) or stained with cresyl violet by standard Nissl-staining procedures. The coverslipped sections were visualized in brightfield (Nissl) or fluorescence (DAPI) microscopy and sections with electrode tracks were photographed in 10 and 20 x magnification.

Analysis

Signals were analyzed using Igor Pro 4.0 (Wavemetrics, Inc.), built-in and custom routines in Spike2 (Cambridge Electronic Design, Ltd.) and custom-written and open-source code in MATLAB (Mathworks Inc.)

Intracellular data analysis

Stimuli were detected manually, and minimal binomial smoothing was performed to diminish noise on occasion. The latency of orthodromic responses was calculated as the time when the response reached 10% of the maximal amplitude of the sigmoidal fit of the rise of the EPSP. The amplitude of the EPSP was calculated as the maximum of this sigmoidal fit, and the slope of the EPSP calculated as the maximum of the differentiation of this fit. A horizontal line was drawn across the response from the base of the early EPSP and the interception of this line by the hyperpolarizing potential was used to calculate the duration of this latter component. Responses to sweeps of five pulse stimulation trains were averaged with an IgorPro algorithm (n=30 per stimulation protocol). The EPSP response magnitude elicited by the stimulation of the reuniens nucleus was computed by computing the area below the curve. Average response areas evoked by pulses 2 through 5 of the train were subsequently normalized by dividing by the response evoked by the first pulse.

Wake, NREM and REM detection

Detection of wake, NREM and REM sleep was based on automated analysis of the mPFC and EMG signals, followed by manual REM scoring using mPFC, EMG and EOG data. For automated detection, the Spike2 script RatSleepAuto, based on rodent recordings (Costa-Miserachs et al.,

2003), was adapted to cat mPFC recordings. Briefly, the mPFC signal was downsampled to 100 Hz and bandpassed in the delta range (1-4 Hz). The mPFC, EMG and the delta-filtered mPFC signals were then squared and the mean of each signal was calculated in 5 second bins. Each 5-second bin was classified as NREM if the mPFC and delta signals exceed the mean + 1 standard deviation (SD) of the signal and if the EMG fell below mean - 1 s.d. All bins other than NREM were initially classified as wake. In the subsequent manual correction, “wake” bins with EMG below mean – 1 s.d. and EOG above mean + 1 s.d. were classified as REM. In the final stage, the 5-second bins were combined into groups of 4 to create 20 second epochs of wake, REM or NREM according to the majority of 5-second bins that comprised the 20 second epoch. Epochs without a majority of either NREM, REM or wake were labelled as “Transition”.

Slow wave, spindle and SWR detection

Slow wave, spindle and SWR detection was based on methodology described previously in Alizadeh et al. (2022) and respectively in Zugaro et al. (2022), Klinzing et al. (2016) and Levenstein et al. (2019). The detection protocol for all three events was restricted to periods of NREM sleep.

The Freely Moving Animal (FMA) toolbox(Zugaro et al., 2022) was used for slow wave and spindle detection. For slow waves, mPFC and reuniens LFP signals were bandpass filtered between 0.5 to 4 Hz using a FIR filter with a filter order corresponding to 3 cycles of the low frequency cut-off. Tentative slow wave events whose positive peaks were greater than 2.5 standard deviations of the signal and whose difference between positive and negative peaks was greater than 4 standard deviations were detected. Slow waves were finally defined as

periods when consecutive positive-to-negative zero crossings of the signal filtered in 0.5-2 Hz occurred between 0.5 and 2 seconds of each other.

For spindles, mPFC and reuniens LFP signals were bandpassed in the spindle frequency band (7-15 Hz) using finite-impulse-response (FIR) filters from the EEGLAB toolbox (Delorme and Makeig, 2004). The instantaneous amplitude of the filtered signal was then computed from its Hilbert transform and the results were smoothed using a 300 ms Gaussian window. Potential spindles were detected as periods when this signal crossed 3 standard deviations (SD) above its mean for 0.5-3 s A threshold of 2.5 SD above the mean was set to detect spindle onset and offset. Events that occurred within 0.5 seconds of each other were merged into a single event. Events longer than 0.5 s and shorter than 3 s were defined as spindles. The largest peak in spindle amplitude was defined as the time of the spindle event.

For SWRs, hippocampal LFP signals were bandpassed in the ripple frequency band (150-200 Hz, FIR filter from the EEGLAB toolbox). The root mean square (RMS) of the filtered signal was then computed and the results were smoothed using a 50 ms Gaussian windows. SWRs were defined as periods when the smoothed RMS crossed 4 standard deviations above the median and stayed crossed for at least 30 ms. The largest peak in SWR amplitude was defined as the time of the SWR event.

Phase-amplitude coupling

Computations of phase-amplitude coupling (PAC) were based on methodology published previously in Alizadeh et al.(Alizadeh et al., 2022), Dehnavi et al.(Dehnavi et al., 2021) and Staresina et al.(Staresina et al., 2015) Time-frequency representations (TFRs) of every

spindle/slow wave event were obtained using the *mtmconvol* function in the FieldTrip toolbox(Oostenveld et al., 2011). Spindle power around the slow wave was estimated using sliding Hanning tapered windows (10 ms steps) with a variable length that included five cycles. To compute coupling, TFRs were then normalized as percentage change from pre-event baseline (-3.5 to -2.5 second before event) for all events. To calculate the modulation of spindle power by slow wave phase, TFR bins around slow waves were averaged across the spindle frequency range and then filtered in the slow wave frequency range. Phase values of this signal were calculated from their Hilbert transform.

Synchronization index and coupling strength

We defined a synchronization index (SI) for each event:

$$SI = \frac{1}{m}\sum_{j=1}^{m} e^{i[\theta_{slow\ wave}(j) - \theta_{spindle}(j)]}$$

where m is the number of time points, $\theta_{slow\ wave}(j)$ represents slow wave phase value at time *j* and $\theta_{spindle}(j)$ represents phase values of spindle power fluctuations at time *j*. Preferred phase was estimated in the interval -0.25 to 0.25s around slow wave peak. The strength of phase-amplitude coupling was estimated from the absolute value of the SI with 1 representing the most consistent phase shift between spindle amplitude and slow wave event. The phase of SI represents the amount of phase shift between the spindle amplitude and slow wave event. Spindle-SWR coupling was computed using a similar procedure. Briefly, the normalized TFRs in the SWR frequency range around each spindle event (baseline defined from -2.5 to -1.5 second before spindle event) were filtered in the spindle frequency range and the SI was defined as the

vector mean of unit vectors, each showing the phase difference between SWR amplitude and slow wave event at different time points around the spindle peak.

Average wavelet transforms

Wavelet transforms of the LFP were calculated using the continuous one-dimensional wavelet transform, estimated by Morse wavelets defined in the *cwt* function, available in the MATLAB wavelet toolbox. Average wavelet transforms around spindle onsets (Figure 2L) were computed using custom-written MATLAB code. First, 5-second LFP epochs, centered on spindle onsets were extracted from the continuous recordings and downsampled to 250 Hz. A filter bank, based on the known epoch length (5 s) and sampling frequency (250 Hz), was created with voices per octave set to 20 and frequency limits set to 0.1 to 50 Hz. Using the filter bank, wavelet transforms of each epoch around a spindle onset were calculated and stored in a 3-dimensional array corresponding to time, frequency, and spindle event. To obtain the magnitude of the signal, the absolute value of the wavelet transform was then computed. To obtain the average wavelet transform of the LFP signals around the spindle event onsets, the mean of the magnitude matrices along the third dimension (spindle events) was calculated.

Spike detection

For spike detection, reuniens LFP signals were bandpass filtered in the 300-8000 Hz range using finite impulse response (FIR) filters from the EEGLAB toolbox. Epochs of ± 250 ms around times when the signal crossed ± 16 SD were considered as artifacts and removed from the analysis. Spikes were detected using UltraMegaSort2000 (Fee et al., 1996) with a negative threshold of -4SD. During a shadow time of 0.75 ms after the threshold crossing, no new event was detected

627 to avoid multiple threshold crossings of one event. A window of 1.5 ms was considered around
628 each detected spike from 0.6 ms before the threshold crossing time to 0.9 ms after this time.

629 Spike sorting was based on a method described previously in Souza et al.(Souza et al., 2019).
630 We first extracted spike features for each channel. The features consisted of peak-to-trough
631 value, trough value and also an index which was set to one for the channel with maximum
632 trough amplitude and zero for the other channels. We used principal component analysis (PCA)
633 to combine 12 features (3 features times 4 channels) and selected the two first components.
634 Gaussian distributions were fitted to PCA components with gaussian mixture model (GMM)
635 algorithm. Each distribution was determined as a potential spike cluster. We further limited the
636 distribution by removing spikes with large Mahalanobis distance from the center of the
637 distribution. We removed, combined, and limited the distributions manually by visual
638 inspection of the plots showing PCA components versus each other and the plots showing the
639 features for different channel pairs (Figure 2 – figure supplement 1). For multi-unit analysis,
640 spikes were detected according to threshold crossing and template matching algorithms in
641 Spike2(CED, 2021). Briefly, fast signals (~1-3 ms) that exceeded the threshold were first
642 detected as putative spikes and timestamped. Thresholds were manually determined according
643 to the signal-to-noise ratio of spikes in each recording. Next, a temporary spike template was
644 formed according to the shape of the putative spike and a “template width” was estimated
645 (twice the mean difference between the template and the spike that created it). Each new spike
646 was then compared against the template and added to it if the spike’s sample points fell within
647 the template width. The template was modified with the addition of each new spike up to a
648 maximum of eight spikes after which the template was checked against previous templates. If a

match was found, the temporary template was merged with the existing template. Otherwise, a new confirmed template was generated.

Peri-event histograms

To analyze reuniens single-unit activity around the onset of SWRs, peri-event spike histograms (PETHs) were calculated for a 1-second period around each event onset and the results were smoothed with a 10 ms Gaussian window. For comparison, surrogate PETHs were obtained by randomly shuffling SWR events detected within 1 second windows. This procedure was repeated 100 times. True-even PETHs were z-score normalized to the firing rate of surrogate PETHs. Single-units with activity greater than 2 SDs and smaller than -2 SDs in the 150 ms window following SWR onset were considered activated and suppressed, respectively.

Phase-locking analysis

For phase-locking analysis, we calculated spindle phase at the time of single-unit spikes occurring within ± 0.25 s around spindle peak (Figure 2H), slow wave phase at SWR time (Figure 3K) and theta phase at single-unit spike time occurring within ± 0.5 s around theta peak (Figure 4C). First, mPFC and reuniens LFPs were filtered in the frequency band of interest (spindle, slow wave, or theta) and the phase of the filtered signal was extracted from its Hilbert transform. These phase values were used to obtain phase histograms and calculate circular means.

Computational model

Our model represents a minimal neural mass model that describes the network architecture required for generating three key oscillatory activities during NREM: the slow oscillation, spindles, and SWRs. The hippocampal-thalamocortical model represents CA1-CA3 networks,

two cortical networks (CX, CX'), and three thalamic networks consisting of mediodorsal nucleus of the thalamus (MD), thalamic reticular nucleus (TRN) and nucleus reuniens (REU). The details of the CA1-CA3, MD-TRN and cortical networks were described previously (Azimi et al., 2021; Ghorbani et al., 2012; Hashemi et al., 2019). In brief, in this neural mass firing rate model, each of cortical and hippocampal networks consists of one identical group of excitatory and one identical group of inhibitory neurons. ${V_k}^m$ and ${N_k}^m$ indicate the membrane potential and the number of type k (either e, excitatory or i, inhibitory) neurons of network m, respectively. The firing rates of hippocampal and cortical neurons as well as the reuniens neurons are sigmoid functions of the membrane potential of the neurons with the sharpness and threshold of g_k^m, V_k^{*m} respectively:

$$r(V_k^m) = r_0 + \frac{r_1}{1 + exp[-(V_k^m - V_k^{*m}) / g_k^m]} \quad , \{m\} \in \{CA3, CA1, CX, CX', REU\} \quad (1)$$

where, r_1 = 70 Hz (r_0 = 0.1 Hz) is the maximal (minimum) firing rate. T-type calcium currents is modeled only for MD and TRN neurons by defining a bursting variable, u_m so that these neurons show burst mode in addition to the tonic mode:

$$r(V_k^m) = \frac{R_k^T}{1+exp[(V_k^m - V_k^T) / g_k^T]}(exp[L_k u_k]) + \frac{R_k^B}{1+exp[(V_k^m - V_k^B) / g_k^B]}(1 - exp[L_k u_k]), \quad \{m\} \in \{\mathrm{MD, TRN}\} \ (2)$$

Here g_k^T (g_k^B) , R_k^T (R_k^B), and V_k^T(V_k^B) show the sharpness of the firing rate dependence on the membrane potential , the maximum firing rate, and the threshold potential during tonic (burst) mode. The sharpness of switch between the two modes is controlled by L_k (a positive parameter).

The probability and the strength of connections from neuron k of network m to neuron j of network n are shown by $P_{kj}^{m\text{-}n}$ and $J_{kj}^{m\text{-}n}$ respectively. m and n can be CA1, CA3, CX , MD , TRN or REU. k and j can take e or i (representing excitatory and inhibitory neurons, respectively). For the short-range connections since m and n are equal, only one of them is shown. E-E connections of cortical and hippocampal excitatory neurons are subject to dendritic spike frequency adaptation so that $J_{ee}^{m}/J_{ee}^{n\text{-}m}$ is a sigmoid function of an adaptation variable, c^m with sharpness and threshold of g_c and c^* respectively:

$$J_{ee}^{m}(c) = \frac{J0_{ee}^{m}}{1 + exp[c - c^*) / g_c]} \qquad (3)$$

Here $J0_{ee}^{m}$ is the maximal synaptic strength. The full model is described by 17 rate equations:

$$\frac{dV_e^{CA3}}{dt} = -\frac{V_e^{CA3}}{\tau_e} + N_e^{CA3} P_{ee}^{CA3} J_{ee}^{CA3}(c^{CA3}) r(V_i^{CA3}) - N_i^{CA3} P_{ie}^{CA3} J_{ie}^{CA3} r(V_i^{CA3}) \qquad (4)$$

$$\frac{dV_i^{CA3}}{dt} = -\frac{V_i^{CA3}}{\tau_I} + N_e^{CA3} P_{ei}^{CA3} J_{ei}^{CA3} r(V_e^{CA3}) - N_i^{CA3} P_{ii}^{CA3} J_{ii}^{CA3} r(V_i^{CA3}) \qquad (5)$$

$$\frac{dc^{CA3}}{dt} = -\frac{c^{CA3}}{\tau_c} + N_e^{CA3} P_{ee}^{CA3} \Delta c^{CA3} r(V_e^{CA3}) \qquad (6)$$

$$\frac{dV_e^{CA1}}{dt} = -\frac{V_e^{CA1}}{\tau_e} - N_i^{CA1} P_{ie}^{CA1} J_{ie}^{CA1} r(V_i^{CA1}) + N_e^{CA3} P_{ee}^{CA3\text{-}CA1} J_{ee}^{CA3\text{-}CA1}(c^{CA1}) r(V_e^{CA3})$$

$$+N_e^{REU} P_{ee}^{REU\text{-}CA1} J_{ee}^{REU\text{-}CA1}(c^{CA1}) r(V_e^{REU}) \qquad (7)$$

$$\frac{dV_i^{CA1}}{dt} = -\frac{V_i^{CA1}}{\tau_I} + N_e^{CA1} P_{ei}^{CA1} J_{ei}^{CA1} r(V_e^{CA1}) + N_e^{CA3} P_{ei}^{CA3\text{-}CA1} J_{ei}^{CA3\text{-}CA1} r(V_e^{CA3}) -$$

$$N_i^{CA1} P_{ii}^{CA1} J_{ii}^{CA1} r(V_i^{CA1}) + N_e^{REU} P_{ei}^{REU\text{-}CA1} J_{ei}^{REU\text{-}CA1} r(V_e^{REU}) \qquad (8)$$

$$\frac{dc^{CA1}}{dt} = -\frac{c^{CA1}}{\tau_c} + N_e^{CA3} P_{ee}^{CA3\text{-}CA1} \Delta c^{CA1} r(V_e^{CA3}) + N_e^{REU} P_{ee}^{REU\text{-}CA1} \Delta c^{CA1} r(V_e^{REU}) \qquad (9)$$

$$\frac{dV_e^{CX}}{dt} = -\frac{V_e^{CX}}{\tau_e} + N_e^{CX} P_{ee}^{CX} J_{ee}^{CX}(c^{CX}) r(V_e^{CX}) - N_i^{CX} P_{ie}^{CX} J_{ie}^{CX} r(V_i^{CX}) + N_e^{'CX} P_{ee}^{CX2\text{-}CX1} J_{ee}^{CX2\text{-}CX1}(c^{CX}) r(V_e^{'CX}) +$$

$$N_e^{REU} P_{ee}^{REU\text{-}CX} J_{ee}^{REU\text{-}CX}(c^{CX}) r(V_e^{REU}) + N_e^{CA1} P_{ee}^{CA1\text{-}CX} J_{ee}^{CA1\text{-}CX}(c^{CX}) r(V_e^{CA1}) \qquad (10)$$

$$\frac{dc^{CX}}{dt} = -\frac{c^{CX}}{\tau_c} + N_e^{CX} P_{ee}^{CX} \Delta c^{CX} r(V_e^{CX}) + N_e^{'CX} P_{ee}^{CX2\text{-}CX1} \Delta c^{CX} r(V_e^{'CX}) + N_e^{REU} P_{ee}^{REU\text{-}CX} \Delta c^{CX} r(V_e^{REU})$$

$$+ N_e^{CA1} P_{ee}^{CA1\text{-}CX} \Delta c^{CX} r(V_e^{CA1}) \qquad (11)$$

$$\frac{dV_i^{CX}}{dt} = -\frac{V_i^{CX}}{\tau_I} - N_i^{CX} P_{ii}^{CX} J_{ii}^{CX} r(V_i^{CX}) + N_e^{CX} P_{ei}^{CX} J_{ei}^{CX} r(V_e^{CX}) + N_e^{'CX} P_{ei}^{CX2\text{-}CX1} J_{ei}^{CX2\text{-}CX1} r(V_e^{'CX}) +$$

$$N_e^{REU} P_{ei}^{REU\text{-}CX} J_{ei}^{REU\text{-}CX} r(V_e^{REU}) + N_e^{CA1} P_{ei}^{CA1\text{-}CX} J_{ei}^{CA1\text{-}CX} r(V_e^{CA1}) \qquad (12)$$

$$\frac{dV_e^{'CX}}{dt} = -\frac{V_e^{'CX}}{\tau_e} - N_I^{'CX} P_{ie}^{'CX} J_{ie}^{'CX} r(V_I^{'CX}) + N_e^{'CX} P_{ee}^{'CX} J_{ee}^{'CX}(c^{'CX}) r(V_e^{'CX}) + N_e^{CX} P_{ee}^{CX1\text{-}CX2} J_{ee}^{CX1\text{-}CX2}(c^{'CX}) r(V_e^{CX}) +$$

$$N_e^{MD} P_{ee}^{'MD\text{-}CX} J_{ee}^{'MD\text{-}CX}(c^{'CX}) r(V_e^{MD}) \qquad (13)$$

$$\frac{dc^{'CX}}{dt} = -\frac{c^{'CX}}{\tau_c} + N_e^{'CX} P_{ee}^{'CX} \Delta c^{'CX} r(V_e^{'CX}) + N_e^{CX} P_{ee}^{CX1\text{-}CX2} \Delta c^{'CX} r(V_e^{CX}) + N_e^{MD} P_{ee}^{'MD\text{-}CX} \Delta c^{'CX} r(V_e^{MD})$$

(14)

$$\frac{dV_I^{'CX}}{dt} = -\frac{V_I^{'CX}}{\tau_I} + N_e^{'CX} P_{ei}^{'CX} J_{ei}^{'CX} r(V_e^{'CX}) - N_I^{'CX} P_{ii}^{'CX} J_{ii}^{'CX} r(V_I^{'CX}) + N_e^{CX} P_{ei}^{CX1\text{-}CX2} J_{ei}^{CX1\text{-}CX2} r(V_e^{CX}) +$$

$$N_e^{MD} P_{ei}^{'MD\text{-}CX} J_{ei}^{'MD\text{-}CX} r(V_e^{MD}) \qquad (15)$$

$$\frac{dV_e^{MD}}{dt} = -\frac{V_e^{MD}}{\tau_{MD}} - \frac{f_e^{max}}{1 + exp[\frac{(u_e + f_e^{th})}{q_e}]} - N_i^{TRN} P_{ie}^{TRN\text{-}MD} J_{ie}^{TRN\text{-}MD} r(V_i^{TRN}) + N_e^{'CX} P_{ee}^{'CX\text{-}MD} J_{ee}^{'CX\text{-}MD} r(V_e^{'CX})$$

(16)

$$\frac{du_e}{dt} = [\frac{1}{\tau_e^u}(b_e - u_e)] \quad \text{if} \quad V_e^{MD} > -0.1\ \text{mV} \quad \text{then} \quad b_e = 0 \quad \text{otherwise} \quad b_e = -200\ \text{mA} \qquad (17)$$

$$\frac{dV_i^{TRN}}{dt} = -\frac{V_i^{TRN}}{\tau_{TRN}} - \frac{f_i^{max}}{1 + exp[\frac{(u_I + f_i^{th})}{q_i}]} - N_i^{TRN} P_{ii}^{TRN} J_{ii}^{TRN} r(V_i^{TRN}) + N_e^{MD} P_{ei}^{MD\text{-}TRN} J_{ei}^{MD\text{-}TRN} r(V_e^{MD}) + N_e^{'CX} P_{ei}^{'CX\text{-}TRN} J_{ei}^{'CX\text{-}TRN} r(V_e^{'CX}) \quad (18)$$

$$\frac{du_i}{dt} = [\frac{1}{\tau_i^{u}}(b_I - u_i)] \qquad \text{if} \quad V_i^{TRN} > 0 \text{ mV} \quad \text{then} \quad b_I = 0 \quad \text{otherwise} \quad b_i = \text{-}200 \text{ mA} \quad (19)$$

$$\frac{dV_e^{REU}}{dt} = -\frac{V_e^{REU}}{\tau_{REU}} - N_i^{TRN} P_{ie}^{TRN\text{-}REU} J_{ie}^{TRN\text{-}REU} r(V_i^{TRN}) + N_e^{CX} P_{ee}^{CX\text{-}REU} J_{ee}^{CX\text{-}REU} r(V_e^{CX}) + N_e^{CA1} P_{ee}^{CA1\text{-}REU} J_{ee}^{CA1\text{-}REU} r(V_e^{CA1}) \quad (20)$$

The nonlinear equations of the model were solved using the fourth-order Runge–Kutta method with a time step of 1 ms by MATLAB R2017b software.

Quantification and statistical analysis

Statistical analyses were performed using the MATLAB Statistics and Machine Learning Toolbox (Mathworks Inc., Natick, MA, USA). Phase analysis was performed using the circular statistics tool box developed by Berens (2009). The Rayleigh test was performed to determine the uniformity in the phase preference of events. The Watson-Williams test was used to test the inequality of phases. Polar plots showing phases, and mean phases were plotted using MATLAB.

Intracellular data was analyzed using JMP 5.01 software. Normality was assessed by normal quantile plots and by the Shapiro-Wilk test. Homogeneity of variance was assessed by Levene's test. Confidence intervals were set at 95% ($p<0.05$). ANOVA was used when data was normally distributed and variance homogeneous, Welch ANOVA when variance was non-homogeneous. To determine group differences in normally distributed data, Tukey's range test was used.

Otherwise, differences were assessed by non-parametric testing (van der Waerden test). Standard deviations are reported as SD and the mean absolute deviation is reported as MAD.

Data and code availability

Further information and requests for resources and reagents should be directed to and will be fulfilled by the Lead Contact, Igor Timofeev (igor.timofeev@fmed.ulaval.ca). Original electrophysiological recordings have been deposited at Mendeley Data and are publicly available as of the date of publication.

The following data sets were generated

Basha, Diellor; Timofeev, Igor (2022), "Natural sleep electrophysiology: mPFC, thalamus, hippocampus", Mendeley Data, V2, doi: 10.17632/4x27jjp9mv.2(Basha and Timofeev, 2022). In the public domain at Mendeley Data, https://data.mendeley.com/datasets/4x27jjp9mv/2.

MATLAB code generated for this study is available at https://github.com/DiellorBasha/MATLAB_for_Electrophysiology and https://github.com/azarmehri/brain-network-interactions.

Tetrodes and stainless-steel electrodes manufactured in-house for this study are available from the lead contact with a completed materials transfer agreement. This study did not generate new unique reagents. Any additional information required to reanalyze the data reported in this paper is available from the lead contact upon request.

Key Resources Table

Key Resources Table				
Reagent type (species) or resource	**Designation**	**Source or reference**	**Identifiers**	**Additional information**
strain, cat (males and females)	Cat	Marshall BioResources	Marshall Cat, domestic short-hair	
software, algorithm	MATLAB	This paper	https://github.com/DiellorBasha/MATLAB_for_Electrophysiology	
software, algorithm	MATLAB	This paper	https://github.com/azarmehri/brain-network-interactions	
software, algorithm	Spike2 9.14	Cambridge Electronic Design	N/A	

software, algorithm	FieldTrip	Oostenveld et al., 2011	N/A	
software, algorithm	CircStat	Berens, P. 2009	N/A	
software, algorithm	UltraMegaSort2000 (ums2k)	Neurophysics Lab, UCSD	https://neurophysics.ucsd.edu/software.php	
software, algorithm	Freely Moving Animal (FMA) Toolbox		https://fmatoolbox.sourceforge.net/	
software, algorithm	LabChart 8	ADI Instruments	N/A	
software, algorithm	IgorPro 7	Wavemetrics	N/A	
software, algorithm	Canvas 11	ACDSee	N/A	
chemical compound, drug	DAPI	Invitrogen	D3571	
other, equipment	AM 3000 amplifiers	A-M systems	N/A	
other, equipment	PowerLab 35 Series Data Acquisition	ADI instruments	N/A	
other, equipment	Neurodata IR-283 amplifiers	Cygnus Technology	N/A	
other, equipment	Tetrodes	Custom, This paper	N/A	

758

References

Alizadeh, Z., Azimi, A., and Ghorbani, M. (2022). Enhancement of hippocampal-thalamocortical temporal coordination during slow-frequency long-duration anterior thalamic spindles. J Neurosci.

Azimi, A., Alizadeh, Z., and Ghorbani, M. (2021). The essential role of hippocampo-cortical connections in temporal coordination of spindles and ripples. Neuroimage *243*, 118485.

Basha, D., and Timofeev, I. (2022). Natural sleep electrophysiology: mPFC, thalamus, hippocampus (Mendeley Data).

Bazhenov, M., Timofeev, I., Steriade, M., and Sejnowski, T.J. (1999). Self-sustained rhythmic activity in the thalamic reticular nucleus mediated by depolarizing GABAA receptor potentials. Nat Neurosci *2*, 168-174.

Beckstead, R.M. (1979). An autoradiographic examination of corticocortical and subcortical projections of the mediodorsal-projection (prefrontal) cortex in the rat. J Comp Neurol *184*, 43-62.

Berens, P. (2009). CircStat: A Matlab Toolbox for Circular Statistics. Journal of Statistical Software *31*.

Bertram, E.H., and Zhang, D.X. (1999). Thalamic excitation of hippocampal CA1 neurons: a comparison with the effects of CA3 stimulation. Neuroscience *92*, 15-26.

Bonjean, M., Baker, T., Lemieux, M., Timofeev, I., Sejnowski, T., and Bazhenov, M. (2011). Corticothalamic feedback controls sleep spindle duration in vivo. J Neurosci *31*, 9124-9134.

Bontempi, B., Laurent-Demir, C., Destrade, C., and Jaffard, R. (1999). Time-dependent reorganization of brain circuitry underlying long-term memory storage. Nature *400*, 671-675.

Cavada, C., Llamas, A., and Reinoso-Suárez, F. (1983). Allocortical afferent connections of the prefrontal cortex in the cat. Brain research *260*, 117-120.

Cavdar, S., Onat, F.Y., Cakmak, Y.O., Yananli, H.R., Gulcebi, M., and Aker, R. (2008). The pathways connecting the hippocampal formation, the thalamic reuniens nucleus and the thalamic reticular nucleus in the rat. Journal of anatomy *212*, 249-256.

Çavdar, S., Onat, F.Y., Çakmak, Y.Ö., Yananli, H.R., Gülçebi, M., and Aker, R. (2008). The pathways connecting the hippocampal formation, the thalamic reuniens nucleus and the thalamic reticular nucleus in the rat. Journal of anatomy *212*, 249-256.

CED (2021). Spike2 Version 10 fo Windows: Spike Sorting (Cambridge, England: Cambridge Electronic Design).

Chang, H.T. (1953). Cortical response to activity of callosal neurons. J Neurophysiol *16*, 117-131.

Chauvette, S., Crochet, S., Volgushev, M., and Timofeev, I. (2011). Properties of Slow Oscillation during Slow-Wave Sleep and Anesthesia in Cats. The Journal of Neuroscience *31*, 14998-15008.

Chauvette, S., Seigneur, J., and Timofeev, I. (2012). Sleep oscillations in the thalamocortical system induce long-term neuronal plasticity. Neuron *75*, 1105-1113.

Contreras, D., and Steriade, M. (1996). Spindle oscillation in cats: the role of corticothalamic feedback in a thalamically generated rhythm. J Physiol *490 (Pt 1)*, 159-179.

Contreras, D., Timofeev, I., and Steriade, M. (1996). Mechanisms of long-lasting hyperpolarizations underlying slow sleep oscillations in cat corticothalamic networks. J Physiol *494 (Pt 1)*, 251-264.

Cornwall, J., Cooper, J.D., and Phillipson, O.T. (1990). Projections to the rostral reticular thalamic nucleus in the rat. Experimental Brain Research *80*, 157-171.
Costa-Miserachs, D., Portell-Cortés, I., Torras-Garcia, M., and Morgado-Bernal, I. (2003). Automated sleep staging in rat with a standard spreadsheet. Journal of neuroscience methods *130*, 93-101.
Degenetais, E., Thierry, A.M., Glowinski, J., and Gioanni, Y. (2003). Synaptic influence of hippocampus on pyramidal cells of the rat prefrontal cortex: an in vivo intracellular recording study. Cereb Cortex *13*, 782-792.
Dehnavi, F., Koo-Poeggel, P.C., Ghorbani, M., and Marshall, L. (2021). Spontaneous slow oscillation-slow spindle features predict induced overnight memory retention. Sleep *44*.
Delorme, A., and Makeig, S. (2004). EEGLAB: an open source toolbox for analysis of single-trial EEG dynamics including independent component analysis. Journal of neuroscience methods *134*, 9-21.
Di Prisco, G.V., and Vertes, R.P. (2006). Excitatory actions of the ventral midline thalamus (rhomboid/reuniens) on the medial prefrontal cortex in the rat. Synapse *60*, 45-55.
Diekelmann, S., and Born, J. (2010). The memory function of sleep. Nature reviews Neuroscience *11*, 114-126.
Dolleman-Van der Weel, M.J., Lopes da Silva, F.H., and Witter, M.P. (1997). Nucleus reuniens thalami modulates activity in hippocampal field CA1 through excitatory and inhibitory mechanisms. J Neurosci *17*, 5640-5650.
Fee, M.S., Mitra, P.P., and Kleinfeld, D. (1996). Automatic sorting of multiple unit neuronal signals in the presence of anisotropic and non-Gaussian variability. J Neurosci Methods *69*, 175-188.
Ferraris, M., Ghestem, A., Vicente, A.F., Nallet-Khosrofian, L., Bernard, C., and Quilichini, P.P. (2018). The Nucleus Reuniens Controls Long-Range Hippocampo-Prefrontal Gamma Synchronization during Slow Oscillations. The Journal of neuroscience : the official journal of the Society for Neuroscience *38*, 3026.
Floresco, S.B., and Grace, A.A. (2003). Gating of hippocampal-evoked activity in prefrontal cortical neurons by inputs from the mediodorsal thalamus and ventral tegmental area. J Neurosci *23*, 3930-3943.
Frankland, P.W., and Bontempi, B. (2005). The organization of recent and remote memories. Nature Reviews Neuroscience *6*, 119.
Fuentealba, P., Crochet, S., Timofeev, I., and Steriade, M. (2004). Synaptic interactions between thalamic and cortical inputs onto cortical neurons in vivo. J Neurophysiol *91*, 1990-1998.
Ghorbani, M., Mehta, M., Bruinsma, R., and Levine, A.J. (2012). Nonlinear-dynamics theory of up-down transitions in neocortical neural networks. Phys Rev E Stat Nonlin Soft Matter Phys *85*, 021908.
Gigg, J., Tan, A.M., and Finch, D.M. (1992). Glutamatergic excitatory responses of anterior cingulate neurons to stimulation of the mediodorsal thalamus and their regulation by GABA: an in vivo iontophoretic study. Cerebral cortex (New York, NY : 1991) *2*, 477-484.
Gigg, J., Tan, A.M., and Finch, D.M. (1994). Glutamatergic hippocampal formation projections to prefrontal cortex in the rat are regulated by GABAergic inhibition and show convergence with glutamatergic projections from the limbic thalamus. Hippocampus *4*, 189-198.

Gioanni, Y., Rougeot, C., Clarke, P.B., Lepouse, C., Thierry, A.M., and Vidal, C. (1999). Nicotinic receptors in the rat prefrontal cortex: increase in glutamate release and facilitation of mediodorsal thalamo-cortical transmission. The European journal of neuroscience *11*, 18-30.

Goldman-Rakic, P.S., Selemon, L.D., and Schwartz, M.L. (1984). Dual pathways connecting the dorsolateral prefrontal cortex with the hippocampal formation and parahippocampal cortex in the rhesus monkey. Neuroscience *12*, 719-743.

Groh, A., Bokor, H., Mease, R.A., Plattner, V.M., Hangya, B., Stroh, A., Deschenes, M., and Acsády, L. (2014). Convergence of Cortical and Sensory Driver Inputs on Single Thalamocortical Cells. Cerebral Cortex *24*, 3167-3179.

Hashemi, N.S., Dehnavi, F., Moghimi, S., and Ghorbani, M. (2019). Slow spindles are associated with cortical high frequency activity. Neuroimage *189*, 71-84.

Herkenham, M. (1978). The connections of the nucleus reuniens thalami: evidence for a direct thalamo-hippocampal pathway in the rat. J Comp Neurol *177*, 589-610.

Hur, E.E., and Zaborszky, L. (2005). Vglut2 afferents to the medial prefrontal and primary somatosensory cortices: a combined retrograde tracing in situ hybridization study [corrected]. J Comp Neurol *483*, 351-373.

Irle, E., and Markowitsch, H.J. (1982). Widespread cortical projections of the hippocampal formation in the cat. Neuroscience *7*, 2637-2647.

Isomura, Y., Sirota, A., Özen, S., Montgomery, S., Mizuseki, K., Henze, D.A., and Buzsáki, G. (2006). Integration and Segregation of Activity in Entorhinal-Hippocampal Subregions by Neocortical Slow Oscillations. Neuron *52*, 871-882.

Jahnsen, H., and Llinás, R. (1984). Electrophysiological properties of guinea-pig thalamic neurones: an *in vitro* study. J Physiol *349*, 205-226.

Jay, T.M., Thierry, A.M., Wiklund, L., and Glowinski, J. (1992). Excitatory Amino Acid Pathway from the Hippocampus to the Prefrontal Cortex. Contribution of AMPA Receptors in Hippocampo-prefrontal Cortex Transmission. Eur J Neurosci *4*, 1285-1295.

Jay, T.M., and Witter, M.P. (1991). Distribution of hippocampal CA1 and subicular efferents in the prefrontal cortex of the rat studied by means of anterograde transport of Phaseolus vulgaris-leucoagglutinin. J Comp Neurol *313*, 574-586.

Klinzing, J.G., Mölle, M., Weber, F., Supp, G., Hipp, J.F., Engel, A.K., and Born, J. (2016). Spindle activity phase-locked to sleep slow oscillations. Neuroimage *134*, 607-616.

Kolmac, C.I., and Mitrofanis, J. (1997). Organisation of the reticular thalamic projection to the intralaminar and midline nuclei in rats. Journal of Comparative Neurology *377*, 165-178.

Latchoumane, C.-F.V., Ngo, H.-V.V., Born, J., and Shin, H.-S. (2017). Thalamic Spindles Promote Memory Formation during Sleep through Triple Phase-Locking of Cortical, Thalamic, and Hippocampal Rhythms. Neuron *95*, 424-435.e426.

Levenstein, D., Buzsáki, G., and Rinzel, J. (2019). NREM sleep in the rodent neocortex and hippocampus reflects excitable dynamics. Nature communications *10*, 2478.

Lipski, J. (1981). Antidromic activation of neurones as an analytic tool in the study of the central nervous system. J Neurosci Methods *4*, 1-32.

Maingret, N., Girardeau, G., Todorova, R., Goutierre, M., and Zugaro, M. (2016). Hippocampo-cortical coupling mediates memory consolidation during sleep. Nature Neuroscience *19*.

Mansvelder, H.D., Mertz, M., and Role, L.W. (2009). Nicotinic modulation of synaptic transmission and plasticity in cortico-limbic circuits. Semin Cell Dev Biol *20*, 432-440.

McKenna, J.T., and Vertes, R.P. (2004). Afferent projections to nucleus reuniens of the thalamus. J Comp Neurol *480*, 115-142.
Nadim, F., and Bucher, D. (2014). Neuromodulation of neurons and synapses. Current Opinion in Neurobiology *29*, 48-56.
Ohtake, T., and Yamada, H. (1989). Efferent connections of the nucleus reuniens and the rhomboid nucleus in the rat: an anterograde PHA-L tracing study. Neurosci Res *6*, 556-568.
Oostenveld, R., Fries, P., Maris, E., and Schoffelen, J.M. (2011). FieldTrip: Open source software for advanced analysis of MEG, EEG, and invasive electrophysiological data. Comput Intell Neurosci *2011*, 156869.
Pirot, S., Glowinski, J., and Thierry, A.M. (1995). Excitatory responses evoked in prefrontal cortex by mediodorsal thalamic nucleus stimulation: influence of anaesthesia. Eur J Pharmacol *285*, 45-54.
Rajasethupathy, P., Sankaran, S., Marshel, J.H., Kim, C.K., Ferenczi, E., Lee, S.Y., Berndt, A., Ramakrishnan, C., Jaffe, A., Lo, M.*, et al.* (2015). Projections from neocortex mediate top-down control of memory retrieval. Nature *526*, 653-659.
Ramanathan, K.R., and Maren, S. (2019). Nucleus reuniens mediates the extinction of contextual fear conditioning. Behav Brain Res *374*, 112114.
Ramanathan, K.R., Ressler, R.L., Jin, J., and Maren, S. (2018). Nucleus Reuniens Is Required for Encoding and Retrieving Precise, Hippocampal-Dependent Contextual Fear Memories in Rats. J Neurosci *38*, 9925-9933.
Reep, R.L., Corwin, J.V., Hashimoto, A., and Watson, R.T. (1987). Efferent connections of the rostral portion of medial agranular cortex in rats. Brain Res Bull *19*, 203-221.
Reinoso-Suárez, F. (1961). Topographischer Hirnatlas der Katze für experimental-physiologische Untersuchungen (Darmstadt: Merck).
Robbins, T.W. (2005). Chemistry of the mind: neurochemical modulation of prefrontal cortical function. J Comp Neurol *493*, 140-146.
Robertson, R.T., and Kaitz, S.S. (1981). Thalamic connections with limbic cortex. I. Thalamocortical projections. J Comp Neurol *195*, 501-525.
Room, P., Russchen, F.T., Groenewegen, H.J., and Lohman, A.H. (1985). Efferent connections of the prelimbic (area 32) and the infralimbic (area 25) cortices: an anterograde tracing study in the cat. J Comp Neurol *242*, 40-55.
Sheroziya, M., and Timofeev, I. (2014). Global intracellular slow-wave dynamics of the thalamocortical system. J Neurosci *34*, 8875-8893.
Siapas, A.G., Lubenov, E.V., and Wilson, M.A. (2005). Prefrontal Phase Locking to Hippocampal Theta Oscillations. Neuron *46*, 141-151.
Siapas, A.G., and Wilson, M.A. (1998). Coordinated interactions between hippocampal ripples and cortical spindles during slow-wave sleep. Neuron *21*, 1123-1128.
Souza, B.C., Lopes-Dos-Santos, V., Bacelo, J., and Tort, A.B.L. (2019). Spike sorting with Gaussian mixture models. Sci Rep *9*, 3627.
Staresina, B.P., Bergmann, T.O., Bonnefond, M., van der Meij, R., Jensen, O., Deuker, L., Elger, C.E., Axmacher, N., and Fell, J. (2015). Hierarchical nesting of slow oscillations, spindles and ripples in the human hippocampus during sleep. Nat Neurosci *18*, 1679-1686.
Steriade, M., Domich, L., Oakson, G., and Deschenes, M. (1987). The deafferented reticular thalamic nucleus generates spindle rhythmicity. J Neurophysiol *57*, 260-273.

Swanson, L.W. (1981). A direct projection from Ammon's horn to prefrontal cortex in the rat. Brain Res *217*, 150-154.
Takagishi, M., and Chiba, T. (1991). Efferent projections of the infralimbic (area 25) region of the medial prefrontal cortex in the rat: an anterograde tracer PHA-L study. Brain research *566*, 26-39.
Tierney, P.L., Dégenètais, E., Thierry, A.M., Glowinski, J., and Gioanni, Y. (2004). Influence of the hippocampus on interneurons of the rat prefrontal cortex. The European journal of neuroscience *20*, 514-524.
Timofeev, I., and Chauvette, S. (2019). Chapter 29 - Sleep-Wake and Cortical Synaptic Plasticity. In Handbook of Behavioral Neuroscience, H.C. Dringenberg, ed. (Elsevier), pp. 443-454.
Timofeev, I., Grenier, F., and Steriade, M. (2001). Disfacilitation and active inhibition in the neocortex during the natural sleep-wake cycle: an intracellular study. Proc Natl Acad Sci U S A *98*, 1924-1929.
Vertes, R.P., Hoover, W.B., Do Valle, A.C., Sherman, A., and Rodriguez, J.J. (2006). Efferent projections of reuniens and rhomboid nuclei of the thalamus in the rat. The Journal of Comparative Neurology *499*, 768-796.
Vertes, R.P., Hoover, W.B., Szigeti-Buck, K., and Leranth, C. (2007). Nucleus reuniens of the midline thalamus: link between the medial prefrontal cortex and the hippocampus. Brain Res Bull *71*, 601-609.
Walsh, D.A., Brown, J.T., and Randall, A.D. (2017). In vitro characterization of cell-level neurophysiological diversity in the rostral nucleus reuniens of adult mice. The Journal of Physiology *595*, 3549-3572.
Williams, G.V., and Goldman-Rakic, P.S. (1995). Modulation of memory fields by dopamine D1 receptors in prefrontal cortex. Nature *376*, 572-575.
Wilson, M.A., and McNaughton, B.L. (1994). Reactivation of hippocampal ensemble memories during sleep. Science *265*, 676-679.
Xu, W., and Sudhof, T.C. (2013). A neural circuit for memory specificity and generalization. Science *339*, 1290-1295.
Yang, M., Logothetis, N.K., and Eschenko, O. (2019). Occurrence of Hippocampal Ripples is Associated with Activity Suppression in the Mediodorsal Thalamic Nucleus. The Journal of Neuroscience *39*, 434.
Zugaro, M., Todorova, R., Girardeau, G., Cei, A., and El Kanbi, K. (2022). FMAToolbox.

Figures

Figure 1 Differential synaptic responses of mPFC neurons to ventral hippocampal and reuniens stimulation

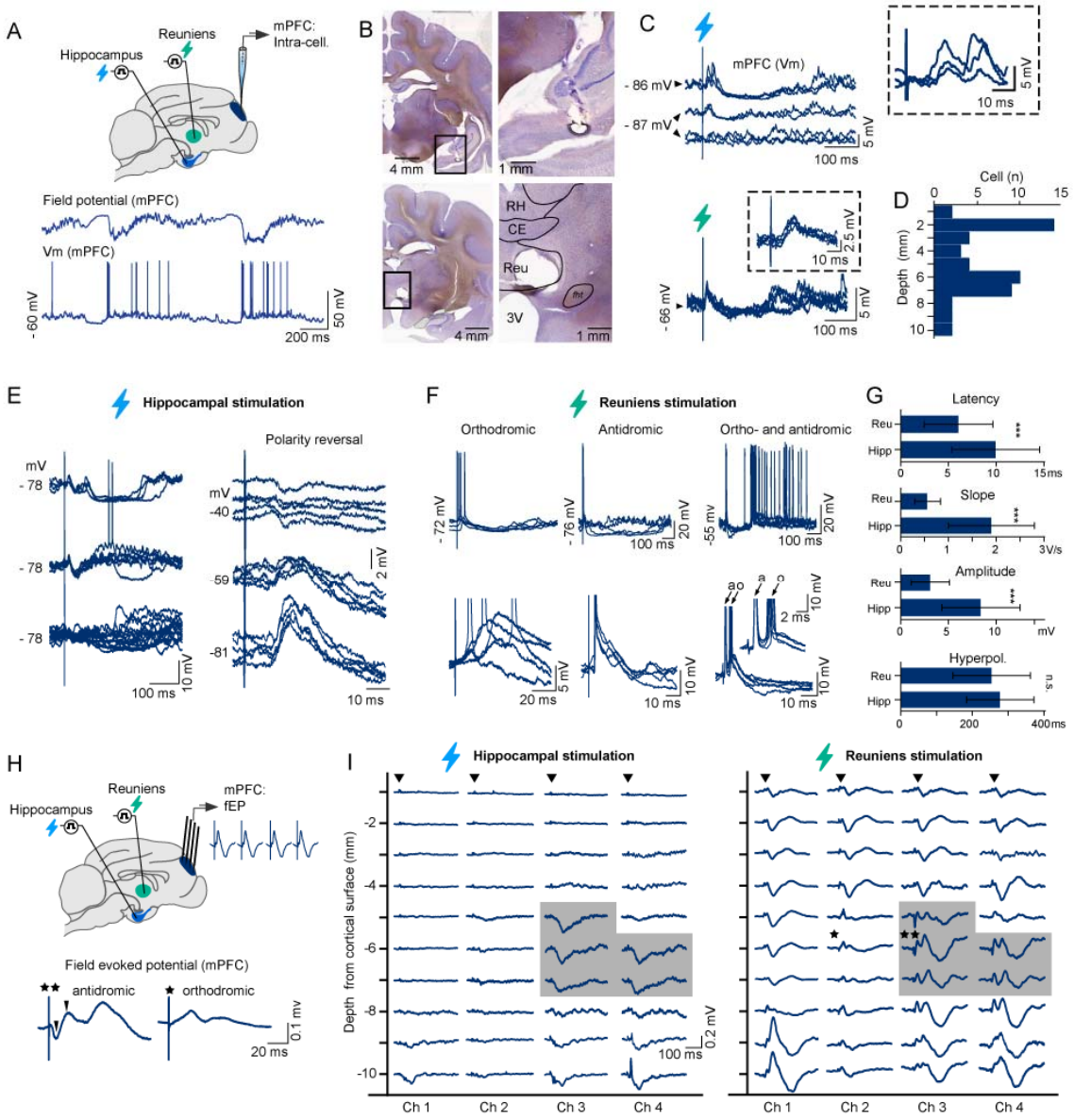

971 A. Schematic of experimental setup: intracellular recordings of the mPFC were
972 obtained in vivo during targeted stimulation of the ventral hippocampus and
973 reuniens (top). Representative segment of intracellular recordings of the mPFC and
974 proximal prefrontal LFP recorded in vivo during anesthesia (bottom).

975 B. Electrolytic lesions at stimulation sites in the ventral hippocampus (top) and midline
976 thalamus (bottom) in Nissl-stained coronal sections.

977 C. mPFC synaptic responses to ventral hippocampal stimulation (top) and reuniens
978 stimulation (bottom), recorded from same neuron, 5.2 mm ventral from the cortical
979 surface. Note, variable, complex responses to hippocampal stimulation (top) and
980 rapid, consistent responses to reuniens stimulation (bottom).

981 D. Location of recorded cells, estimated according to the dorsoventral position of the
982 recording pipette with respect to the cortical surface.

983 E. Heterogeneous postsynaptic potential responses of a single mPFC neuron to
984 consecutive ventral hippocampal stimulation (left): early double depolarizing
985 response (top), early single response (middle), and no response (bottom). Reversal
986 of early response with progressive depolarization (right), indicates involvement of
987 $GABA_A$-mediated inhibition (n=5 pulses at each voltage).

988 F. Intracellular responses to single pulse stimulation of the reuniens nucleus were
989 orthodromic (left, n=17 neurons), antidromic (middle, n=2 neurons) or both
990 orthodromic and antidromic (right, n=1 neuron), consistent with bidirectional

991 connectivity between the reuniens and the mPFC. Jitter in response latency
992 characterized orthodromic spikes (bottom, left), compared to the consistent timing
993 of antidromic spikes (bottom, middle) that were further confirmed with collision
994 tests (not shown).

995 G. Population data (n=49 neurons from 15 acute animals, mean ± SD), depicting the
996 response properties of mPFC neurons to ventral hippocampal and reuniens
997 stimulation: response latency (6.05±3.6 ms and 9.95±4.6 ms for reuniens and
998 hippocampal stimulation, respectively, t-test, $p<0.01$), response amplitude (3.1±2.0
999 mV and 8.4±4.1 mV for reuniens and hippocampal stimulation, respectively, t-test,
1000 $p<0.01$), slope of the early postsynaptic potential (0.56±0.27 V/s and 1.9±0.9 V/s for
1001 reuniens and hippocampal stimulation, respectively, t-test, $p<0.01$) and duration of
1002 the late, hyperpolarizing component (254±108 ms and 278±94 ms for reuniens and
1003 hippocampal stimulation, respectively, $p=0.2$, t-test).

1004 H. Schematic of experimental setup illustrating targeted stimulation of the ventral
1005 hippocampus and reuniens and field responses recorded from the mPFC at 1 mm
1006 intervals along the medial wall of the pericruciate gyrus, prefrontal cortex (top).
1007 Evidence for antidromic field responses elicited by reuniens stimulation: short-
1008 latency, depth-negative events (bottom, left) compared to orthodromic responses
1009 lacking this event (bottom, right).

1010 I. Topography of mPFC responses to hippocampal and reuniens stimulation.
1011 Stimulation of the reuniens evoked field responses in a wider prefrontal territory

than ventral hippocampal stimulation. Traces show the average mPFC field response to 10 pulses (0.2 ms, 0.3-1.5 mA at 1 Hz). Regions where ventral hippocampal stimulation elicited responses overlapped with regions where reuniens stimulation elicited antidromic responses (grey shading, stars indicate traces expanded in Figure 1H, bottom). Ch1 was the most anterior electrode and was inserted at AP26. Channels were 1 mm apart in the antero-posterior axis.

Data are presented as mean ± SD; *p < 0.05, **p <0.01, ***p<0.001 (paired t-tests). *Reu - reuniens, RH – rhomboid, CE – central, pars medialis, fht – hypothalamic-tegmental fasciculus*

1022 **Figure 2 Reuniens activity and ventral hippocampal SWRs precede the onset of mPFC spindles**

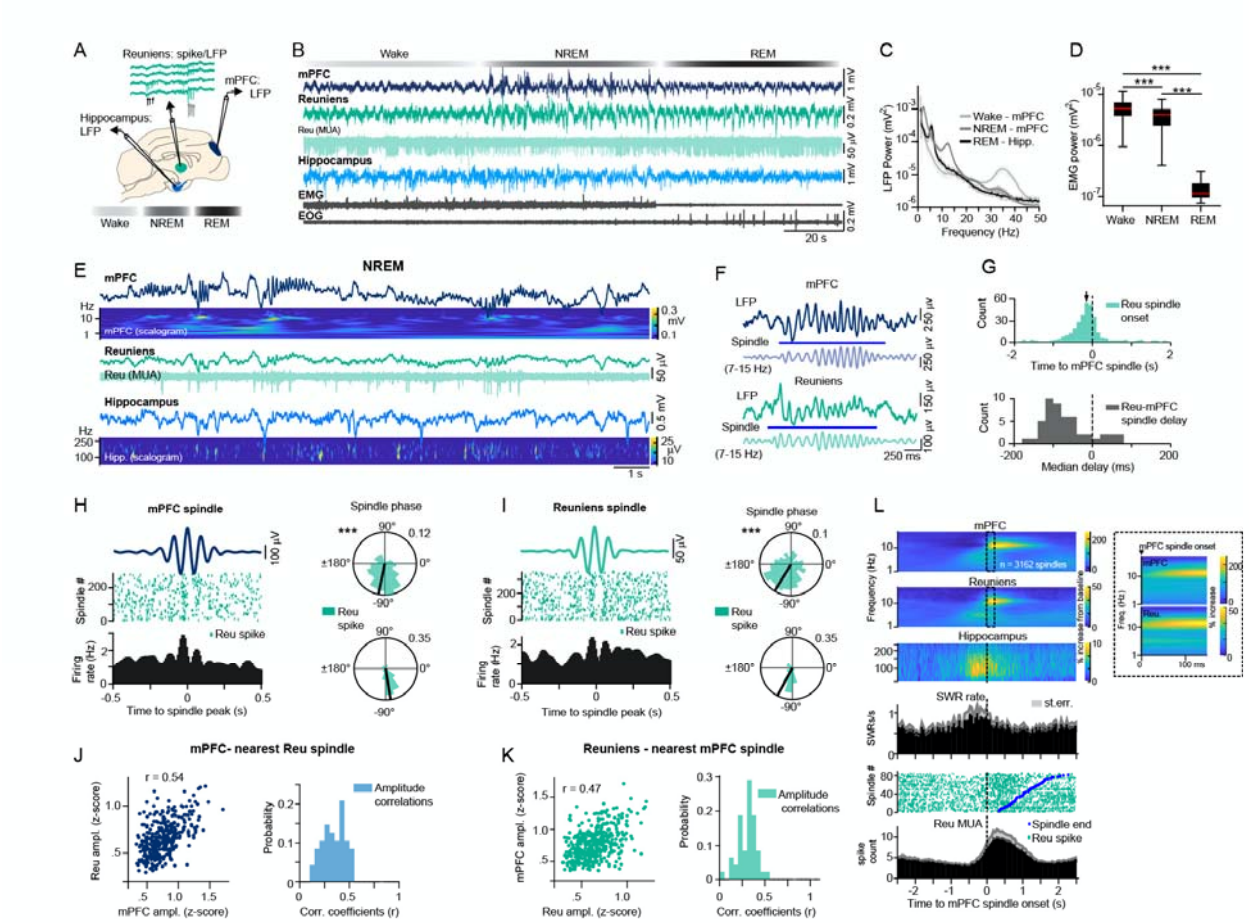

1023

1024 A. Schematic of experimental setup illustrating LFP recordings of the ventral hippocampus

1025 and mPFC and targeted spike/LFP recordings of the reuniens during natural sleep.

1026 B. A segment of LFP recordings of the mPFC, reuniens and ventral hippocampus during

1027 wake, NREM and REM states. For simplicity, we have chosen a segment with wake

1028 followed by unusually short NREM, followed by REM. Sleep/wake states were detected

1029 according to mPFC delta (1-4 Hz) power, mPFC signal amplitude and nuchal muscle

1030 activity (EMG).

1031 C. The average power spectrum of LFP recordings in detected states, showing high gamma
1032 power in the mPFC during wake, high delta, and spindle power in the mPFC during
1033 NREM and high theta power in the ventral hippocampus during REM (n=52 recording
1034 sessions from 4 animals).
1035 D. Muscle activity in detected wake, NREM and REM states. The red line in boxplot
1036 indicates the median, box limits represent the first and third quartile and whiskers
1037 indicate data range. ***$p<0.001$; *post-hoc* Tukey test after one-way ANOVA, n=52
1038 recording sessions (4 chronic animals).
1039 E. Representative segment of LFP recordings during NREM with corresponding wavelet
1040 transforms of the signal, showing the correlated activity of mPFC slow waves, spindles,
1041 ventral hippocampal SWRs (top and bottom) and reuniens multi-unit activity (middle).
1042 The frequency axes for wavelet transforms are plotted in logarithmic scale.

1043 F. Representative example of overlapping reuniens and mPFC spindles. Blue lines indicate
1044 automatically detected spindles in reuniens and mPFC LFPs.

1045 G. The relative onset of reuniens spindles with respect to the onset of mPFC spindles in 100
1046 ms bins (top). The black arrow indicates the median delay time (median ± mean
1047 absolute deviation [MAD] = -0.147±0.556s, Wilcoxon signed rank test, $p = 6.13 \times 10^{-15}$,
1048 n=346). The distribution of median delay times between each reuniens-mPFC spindle
1049 pair for each recording in 20 ms bins (bottom, median = -0.083 s, n=49 sessions).

1050 H. Reuniens single-unit activity relative to the phase of mPFC spindle cycles, aligned to
1051 mPFC spindle peaks. The average prefrontal LFP during spindles, filtered in the spindle

1052 frequency range (top left). Spike raster and the associated peri-event histogram of a
1053 representative reuniens single-unit during the above mPFC spindle (bottom left, 10 ms
1054 bins). Phase-locking of the same reuniens single-unit to mPFC spindle cycles (top right,
1055 n=351 phases, $p = 9.120 \times 10^{-29}$, Rayleigh test) and the mean phase preference of all
1056 significantly modulated reuniens single-units (bottom right, n= 24/49 single-units from 4
1057 chronic animals, mean ± SD = -80.87 ± 41.64°, $p = 2.942 \times 10^{-7}$, Rayleigh test).

1058 I. Reuniens single-unit activity relative to the phase of reuniens spindle cycles. Same
1059 analysis as in H but referenced to reuniens spindles in one session (n=451 phases, p =
1060 8.048×10^{-18}, Rayleigh test) and population data (n= 29/49 single-units from 4 chronic
1061 animals, mean ± SD = -118.25 ± 47.72°, $p = 1.047 \times 10^{-6}$, Rayleigh test). Polar histograms
1062 indicate the normalized count of LFP phases at spike time. The black line indicates the
1063 mean phase angle of the associated histogram. Spikes occurred at earlier phases
1064 referenced to reuniens spindles compared to mPFC spindles (p = 0.010, Watson-
1065 Williams test).

1066 J. The amplitude of spindles detected in the mPFC versus the amplitude of the nearest
1067 reuniens spindle in one recording session (top, n=343 spindles, r=0.54, $p = 3.22 \times 10^{-27}$,
1068 Pearson correlation) and the value of coefficients (r) in mPFC-reuniens amplitude
1069 correlations for all sessions (bottom, n=48 sessions with at least 50 spindles).

1070 K. The amplitude of spindles detected in the reuniens versus the amplitude of the nearest
1071 mPFC spindle in one recording session (top, n=428 spindles, r=0.47, $p = 8.61 \times 10^{-25}$,

1072 Pearson correlation) and the value of coefficients (r) for reuniens-mPFC amplitude

1073 correlations for all sessions (n= 48 sessions with at least 50 spindles).

1074 L. The average change in LFP power during mPFC spindles (n=3162) relative to baseline,

1075 referenced to spindle onset, showing increased ventral hippocampal ripple power, and

1076 increased reuniens spindle power prior to the onset of spindles in the mPFC (top).

1077 Histogram of SWR rate in the same time window, referenced to the onset of the same

1078 mPFC spindles as above (middle). Compared to shuffled data, SWR rate was significantly

1079 higher in the 250 ms window prior to the onset of mPFC spindles (t-test, $p<0.05$). Raster

1080 of reuniens multi-unit activity for a single recording session (n=86 spindles) and the

1081 population peri-event histogram (n=3162 spindles), referenced to the onset of mPFC

1082 spindles. Grey in histograms represents standard error.

1083 See also Figure 2 -figure supplement 1 for unit detection.

1084

1085

Figure 3 Slow wave-spindle and slow wave-SWR coupling in the mPFC-reuniens-hippocampal network

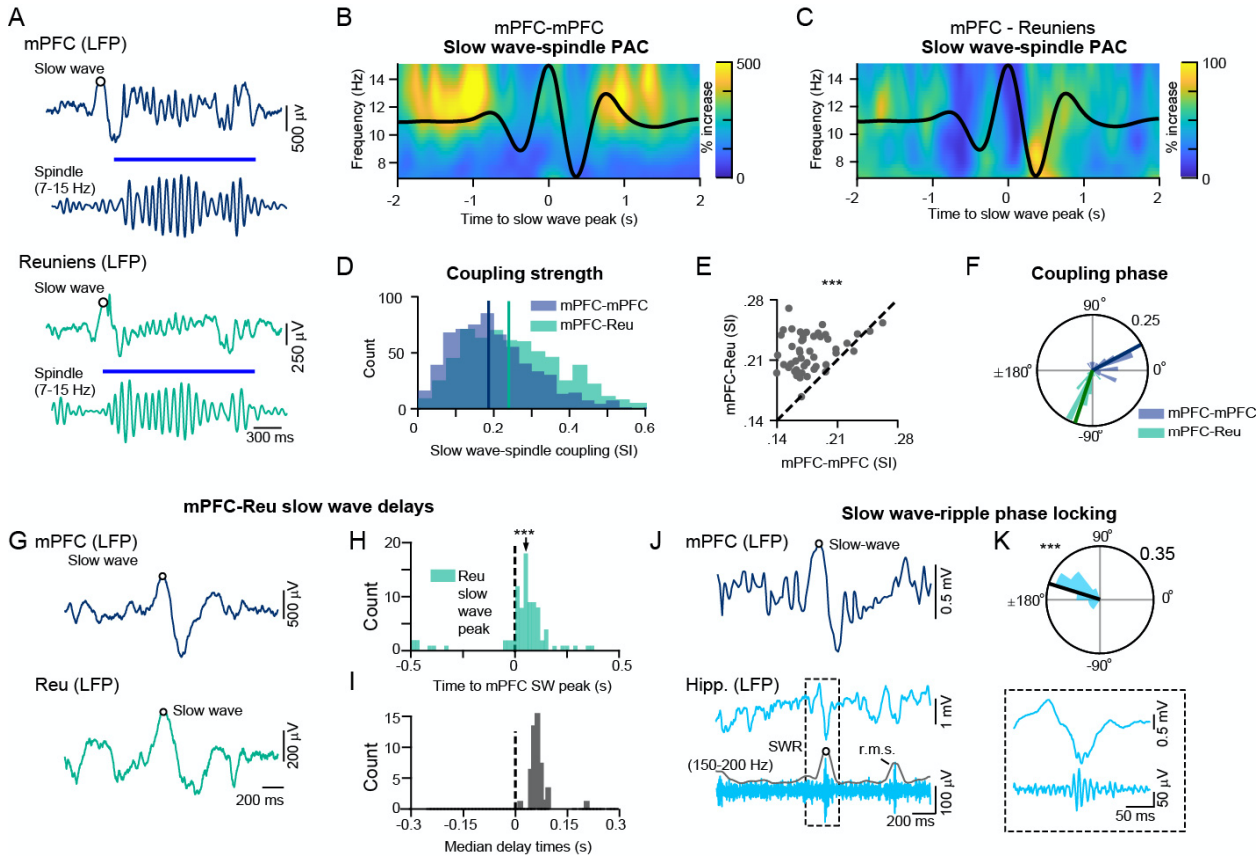

A. A single trial of a slow wave-spindle event, showing raw and filtered for spindle LFP traces of the mPFC (top) and reuniens (bottom).

B. Phase-amplitude coupling (PAC) of mPFC spindles and mPFC slow waves, shown as the average time-frequency representation of mPFC amplitudes in the spindle frequency range, locked to the peak of the mPFC slow wave (percentage change from pre-event baseline, n = 626 slow waves).

1095 C. Phase-amplitude coupling of reuniens spindles and mPFC slow waves, shown as the
1096 average time-frequency representations of reuniens amplitudes, locked to the peak of
1097 the same mPFC slow waves as in B (percentage change from pre-event baseline, n = 626
1098 slow waves). Black curves in B and C show the average of the mPFC LFP, filtered in the
1099 slow wave frequency range (0.5-2Hz).

1100 D. Histogram of slow wave–spindle coupling strengths for mPFC slow waves-mPFC spindles
1101 (blue) and mPFC slow wave-reuniens spindles (green). Vertical lines indicate the median
1102 of the distributions (median ± MAD, SI strength = 0.18 ± 0.09 and 0.24 ± 0.11 for mPFC
1103 and reuniens spindles, respectively, $p = 2.126 \times 10^{-17}$, Wilcoxon signed rank test).

1104 E. Slow wave-spindle coupling strength of mPFC-mPFC pairs versus mPFC-reuniens pairs (n
1105 = 49 sessions, $p = 3.39 \times 10^{-2}$, Wilcoxon signed rank test). Each circle represents one
1106 session.

1107 F. Population data showing the relative preference of spindles to the phase of the mPFC
1108 slow wave, shown as a histogram of SI angle means for mPFC slow wave- mPFC spindle
1109 coupling and mPFC slow wave-reuniens spindle coupling (mean ± SD = 27.92 ± 37.59°, p
1110 $= 4.661 \times 10^{-9}$, n=26 and mean ± SD = -108.48 ± 21.17°, $p = 1.278 \times 10^{-20}$, n = 36, for
1111 mPFC and reuniens respectively, Rayleigh test).

1112 G. A single trial of an overlapping slow waves, showing raw and filtered LFP traces of the
1113 mPFC (top) and reuniens (bottom). Circles indicate slow wave peaks.

1114 H. Single session data, showing the distribution of delays between reuniens and mPFC slow

1115 waves (vertical dashed line). Reuniens slow waves lagged mPFC slow waves (median ±

1116 MAD = 0.126 ± 0.043 s, $p = 3.66 \times 10^{-15}$, n = 82, Wilcoxon signed rank test).

1117 I. Population data of median delay times between each reuniens-mPFC slow wave pair

1118 (n=49 sessions, median of the distribution = 0.136 s).

1119 J. Single-trial of raw mPFC and raw and filtered for ripples ventral hippocampal LFPs

1120 during one overlapping slow wave-SWR event. Inset shows an expanded view of the

1121 detected SWR.

1122 K. Circular histogram of mPFC slow wave phases at the time of SWRs (mean phase ± SD =

1123 162.7 ± 29.37°, $p = 5.02 \times 10^{-6}$, Rayleigh test).

1124 *p < 0.05, **p <0.01, ***p<0.001.

1125 See also Figure 3 – figure supplement 1 for spindle-SWR coupling.

1126

1127

1128

1129 **Figure 4 Ventral hippocampal theta oscillations and SWRs modulate reuniens activity**

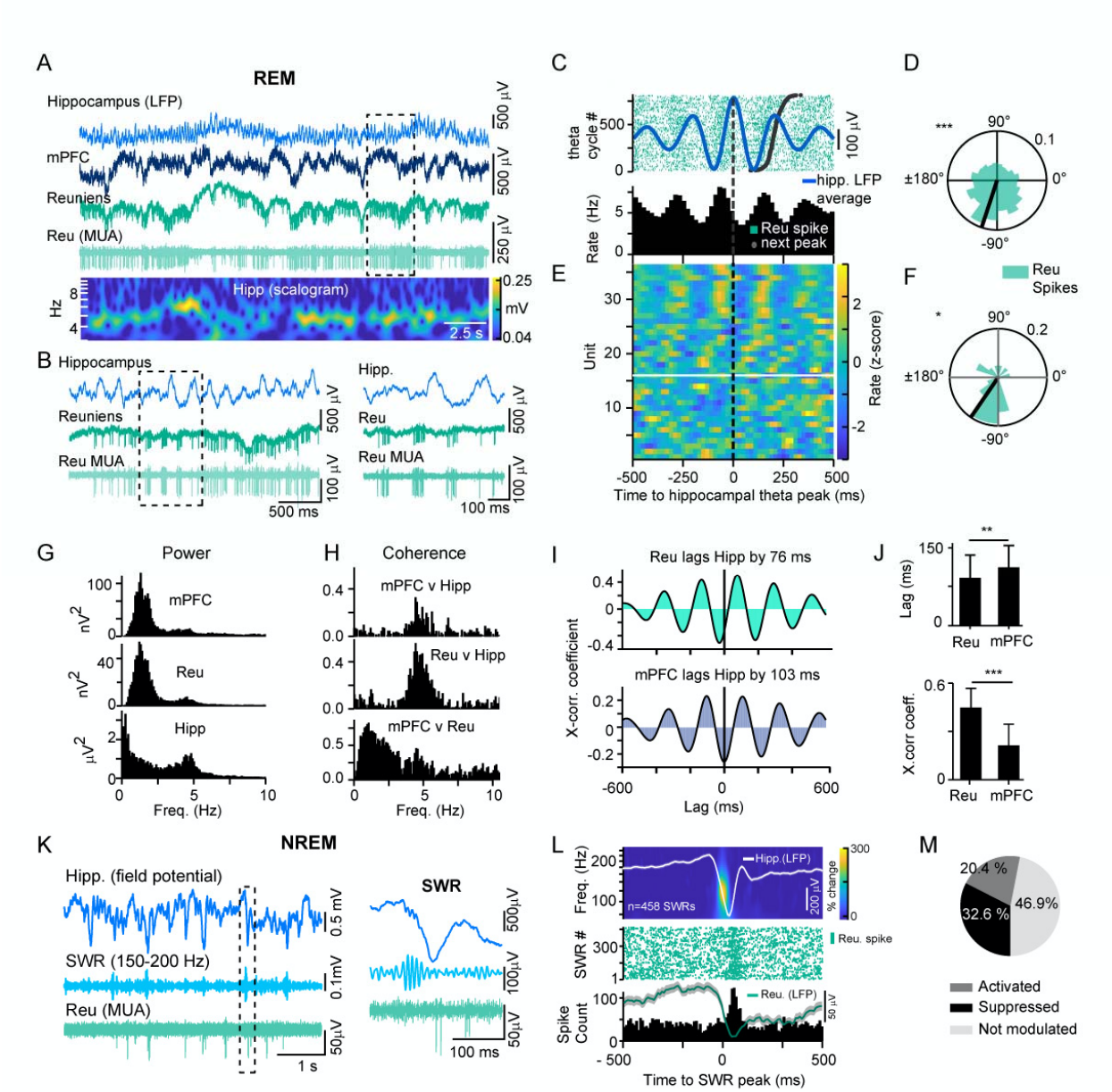

1130

1131 A. Representative example of LFP recordings of the ventral hippocampus, mPFC and

1132 reuniens during REM sleep (top three traces) and the bandpassed (300-8000 Hz) trace of

1133 the reuniens signal showing multiunit activity. Wavelet spectrogram of the hippocampal

1134 trace, showing prominent theta-band activity during REM. The frequency axis is
1135 logarithmic.

1136 B. Expanded view of the recording epoch in the dotted-line box in panel A (left), further
1137 expanded in time (right), showing occasional locking of reuniens multi-unit activity to
1138 ventral hippocampal theta cycles.

1139 C. Peri-event histogram of a representative reuniens single-unit, referenced to the peak of
1140 ventral hippocampal theta cycles (top). The raster is ordered according to the peak-to-
1141 peak latency, with short periods at the bottom and long periods at the top. Dark black
1142 dots indicate the timing of the next peak in the trial. The light blue trace is the average
1143 waveform of the hippocampal LFP.

1144 D. Circular histogram of theta phase at the time of reuniens spikes, showing significant
1145 phase-locking of a reuniens single-unit activity to ventral hippocampal theta cycles
1146 (same single-unit as in C, n = 5207 spikes, $p<10^{-20}$, Rayleigh test).

1147 E. Population data, showing peri-event histograms referenced to the peak of ventral
1148 hippocampal theta cycles as in B (n=36 single units). Units above the white line were
1149 significantly modulated by hippocampal theta cycles.

1150 F. Population data, showing the circular distribution of reuniens firing relative to theta
1151 cycles for all modulated single units (n = 21/36 single-units, mean ± SD = -124.5 ± 59.8 °,
1152 p = 0.011, Rayleigh test).

1153 G. Single session data, showing power spectra of mPFC, reuniens and ventral hippocampal
1154 signals during REM with prominent peaks in the theta range.

1155 H. Single session data, showing signal coherence between mPFC-hippocampus, reuniens-
1156 hippocampus and mPFC-reuniens recording pairs during REM.

1157 I. Single session data, showing cross-correlations and relative time lags of reuniens-
1158 hippocampus and mPFC-hippocampus recording pairs during REM.

1159 J. mPFC signals lagged ventral hippocampal theta signal by longer delay than reuniens
1160 signals lagged hippocampus (top, mean lag ± SD = 87.8 ± 55.5 ms and 109.1 ± 41.52 for
1161 reuniens and mPFC, respectively, n=20 sessions, p=0.002, t-test). Peak cross-correlation
1162 coefficients were significantly higher for reuniens-Hippocampus recording pairs than for
1163 reuniens-mPFC (bottom, mean peak value ± SD = 0.44 ± 0.13 and 0.22 ± 0.07 for
1164 reuniens and mPFC respectively=20 sessions, t-test, $p<10^{-20}$).

1165 K. Representative LFP recordings of the ventral hippocampus and of reuniens multiunit
1166 activity during NREM sleep. Light blue traces show the bandpass filtered hippocampal
1167 recording in the ripple band (150-200 Hz). Light green shows multiunit activity in
1168 reuniens during SWR. Expanded view of a single SWR from the recording epoch in the
1169 dotted-line box and multiunit activity in reuniens.

1170 L. Peri-event analysis of reuniens spiking activity around SWRs in one recording session.
1171 The time frequency representation shows the mean wavelet transform of 458 detected
1172 SWRs, estimated by Morlet wavelets (top). Overlayed traces show the grand average

1173 LFP in the ventral hippocampus (white) and reuniens (green), referenced to the onset of

1174 the SWR. Raster of reuniens spikes (every 10th sweep) and associated peri-event spike

1175 histogram, referenced to the onset of the SWR (bottom).

1176 M. Proportion of reuniens single-units modulated by SWRs (10/49 activated, 16/49

1177 suppressed).

1178 *$p < 0.05$, **$p < 0.01$, ***$p < 0.001$.

1179

1180

Figure 5 Multiregional temporal interactions during NREM sleep events in a hippocampal-thalamocortical model

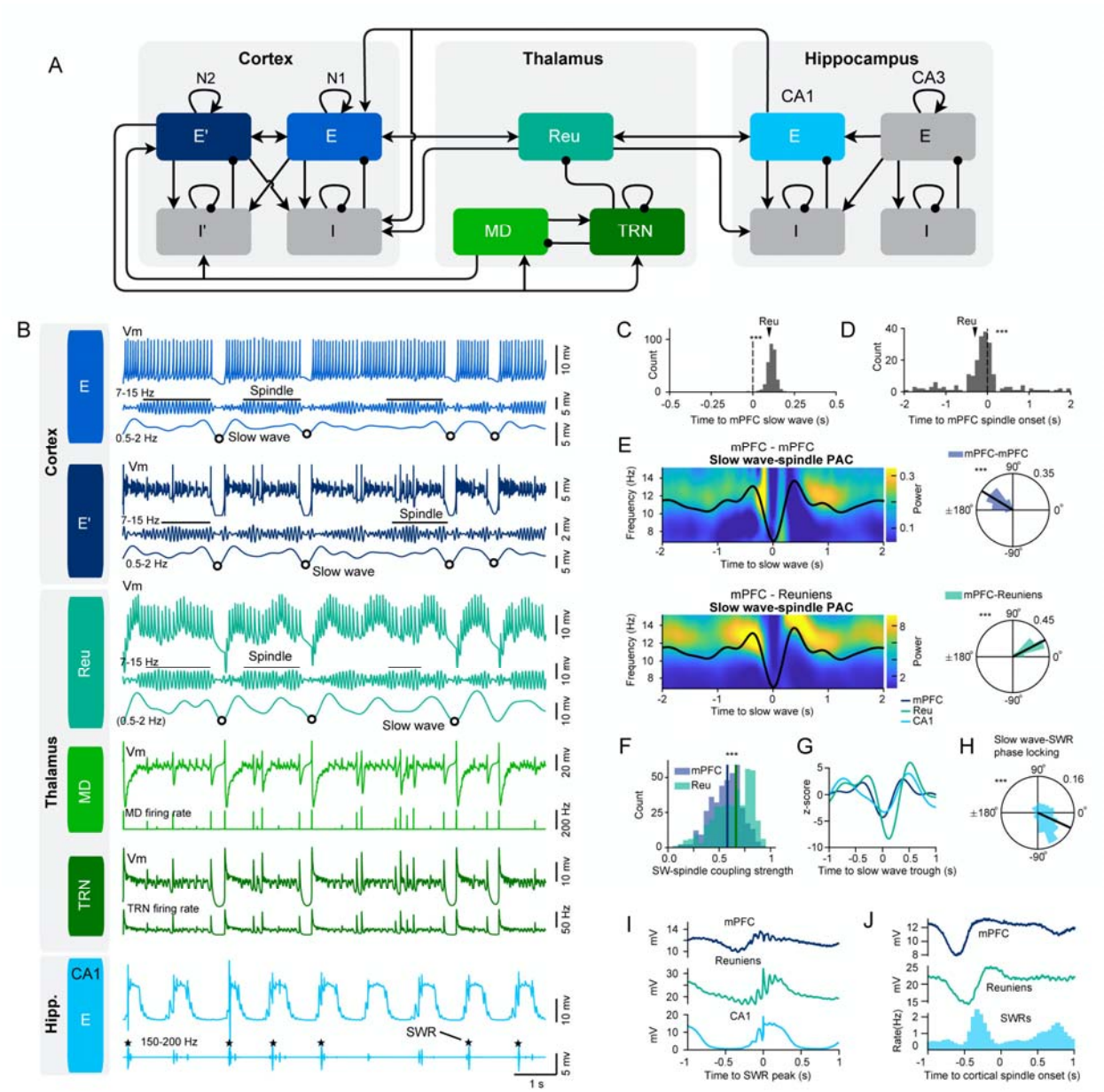

A. The model is composed of two cortical networks (N 1 & 2, representing mPFC layers 5 and 6 respectively), two hippocampal (CA1-CA3) networks and three thalamic nuclei. The three thalamic networks represent the nucleus reuniens (Reu), mediodorsal

1187 thalamic nucleus (MD) and thalamic reticular nucleus (TRN). The cortical and
1188 hippocampal networks are composed of one group of identical excitatory (E) and one
1189 group of identical inhibitory (I) neurons. Excitatory synaptic connections are shown by
1190 arrows and inhibitory connections are indicated as lines ending in a dot.

1191 B. From top to bottom: broadband and filtered (7-15 Hz, 0.5-2 Hz) traces of the membrane
1192 potential of excitatory neurons of cortical network 1 (light blue) and 2 (dark blue) with
1193 detected spindles (black horizontal lines) and slow waves (circles); broadband and
1194 filtered (7-15 Hz, 0.5-2 Hz) traces of the membrane potential of reuniens neurons (blue-
1195 green) with detected spindles and slow waves; broadband trace of the membrane
1196 potential and firing rate of MD (light green) and reticular neurons (dark green);
1197 broadband and filtered (150-200 Hz) traces of the membrane potential of excitatory
1198 neurons of the CA1 network (light blue) with detected SWRs (stars).

1199 C. Distribution of thalamic slow wave troughs (down states) locked to the cortical slow
1200 wave trough (vertical dashed line at zero) occurring within ±0.5 s plotted in 20 ms bins in
1201 the model. The arrow indicates the median of the distribution (n = 277, median ± MAD =
1202 0.113 ± 0.019 s). Thalamic slow waves occur significantly later than cortical slow waves
1203 ($p < 10^{-20}$, Wilcoxon signed rank test).

1204 D. Distribution of thalamic spindle onsets locked to the cortical spindle onset (vertical
1205 dashed line at zero) occurring within ±2 s plotted in 100 ms bins for one session. The
1206 arrow indicates the median of the distribution (n = 211, median ± MAD = -0.102 ± 0.387

1207 s). Thalamic spindles occur significantly earlier than cortical spindles ($p = 1.30 \times 10^{-7}$,

1208 Wilcoxon signed rank test).

1209 E. Phase-amplitude coupling (PAC) of slow waves and spindles, calculated from the

1210 average time-frequency representation of amplitudes in the spindle frequency range,

1211 locked to the trough of the mPFC slow wave. Left, average of cortical slow wave trough-

1212 locked time-frequency representations (n =391) of the membrane potential of mPFC

1213 excitatory neurons (top) and reuniens neurons (bottom). Black curves represent grand

1214 average filtered membrane potential of cortical excitatory neurons in the slow wave

1215 frequency range (0.5-2 Hz) aligned to the cortical slow wave trough (time 0). Right,

1216 circular histogram of synchronization index (SI) angles of cortical (top) and reuniens

1217 (bottom) spindles relative to the cortical slow waves. SI angles were nonuniformly

1218 distributed (mean ± SD = 148.7 ± 23.9°, $p < 10^{-20}$ and mean ± SD = 27.4 ± 20.4°, $p < 10^{-20}$,

1219 for mPFC and reuniens respectively, Rayleigh test, n=391 slow waves).

1220 F. Histogram of the slow wave–spindle coupling strengths (the absolute value of the

1221 synchronization index) for mPFC (blue) and reuniens (green) spindles. Vertical lines

1222 show the median of the distribution ($p = 8.45\times 10^{-9}$, Wilcoxon signed rank test, median

1223 ± MAD SI strength = 0.58 ± 0.11 and 0.66 ± 0.15 for mPFC and reuniens, respectively).

1224 G. Average filtered membrane potential of cortical, reuniens and CA1 excitatory neurons,

1225 in the slow wave frequency range (0.5-2 Hz), aligned to the cortical slow wave trough

1226 (time 0).

1227 H. Distribution of slow wave phases at the time of the SWRs. Zero phase shows the peak

1228 (up state) of slow waves (n = 714, mean ± SD = -24.97 ± 62.01°, $p < 10^{-20}$, Rayleigh test).

1229 I. Average membrane potential of the mPFC, reuniens and CA1 excitatory neurons aligned

1230 to the SWR peaks.

1231 J. Average membrane potential of the mPFC (top) and reuniens (middle) neurons and

1232 histogram of SWR incidence (bottom), aligned to the onset of cortical spindles.

1233 *p < 0.05, **p <0.01, ***p<0.001.

1234

1235

Figure 6 Bidirectional projections between the reuniens and CA1 control multiregional interactions

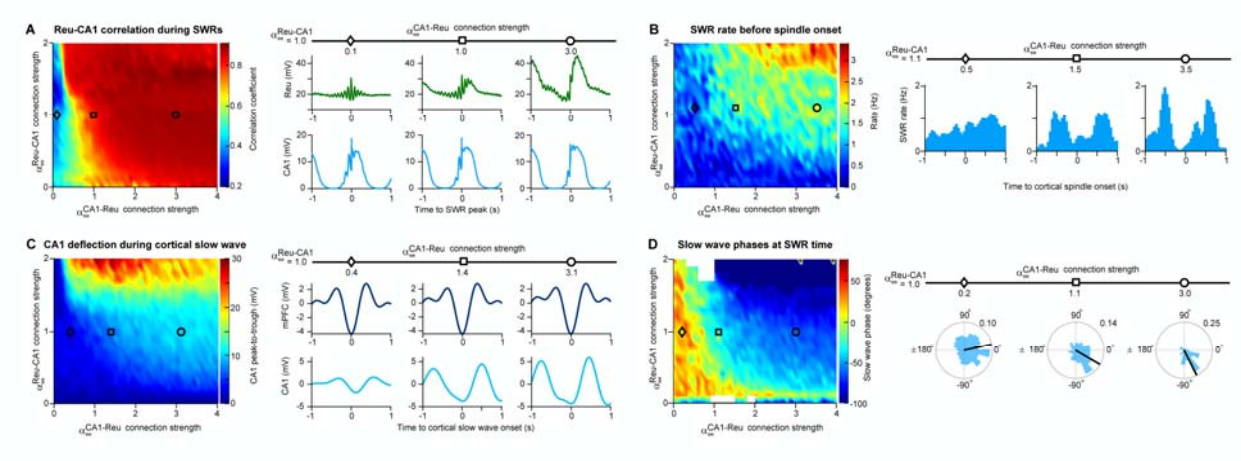

A. Left, correlation between reuniens and CA1 membrane potentials during SWRs (maximum value of the covariance between reuniens and CA1 membrane potentials ± 0.5 s around the SWR peak) versus the CA1-reuniens and reuniens-CA1 connection strengths (and show the factor multiplied to and representing the strength of the input from CA1 to reuniens and from reuniens to excitatory neurons of CA1 respectively. = = 1 corresponds to the network shown in **Figure 5**). Right, average traces of the reuniens and CA1 membrane potentials aligned to the SWR peaks for 3 different values of CA1-reuniens connection strengths.

B. Left, SWR rate preceding the cortical spindle onset (peak-to-trough of the histogram of SWR incidence in a window of -1 s before the spindle onset) versus the CA1-reuniens and reuniens-CA1 connection strengths. Right, histogram of SWR incidence time-locked

to the onset of cortical spindles for 3 different values of CA1-reuniens projection strengths.

C. Left, peak-to-trough of the CA1 deflections around cortical slow wave trough (± 1 s) versus the CA1-reuniens and reuniens-CA1 connection strengths. Right, average filtered membrane potential of cortical, and CA1 excitatory neurons, in the slow wave frequency range (0.5-2 Hz) aligned to the cortical slow wave trough (time 0) for 3 different values of CA1-reuniens connection strengths.

D. Left, mean slow wave phase at the time of SWRs versus the CA1-reuniens and reuniens-CA1 connection strengths. Mean phases are shown only for bins with nonuniformly distributed of phases ($p < 0.05$, Rayleigh test) and omitted for uniformly distributed phase (white boxes). Right, histogram of slow wave phases at the time of SWRs for 3 different values of CA1-reuniens connection strengths, showing decreasing mean phase with increasing CA1-reuniens connections strength ($p = 4.28 \times 10^{-8}$, $p = 7.53 \times 10^{-15}$ and $p = 2.53 \times 10^{-39}$ for $\alpha_{ee}^{CA1-Reu}$ = 0.2, 1.1 and 3.0, respectively).

Figure 2 – figure supplement 1 Single-unit detection method from tetrode recordings

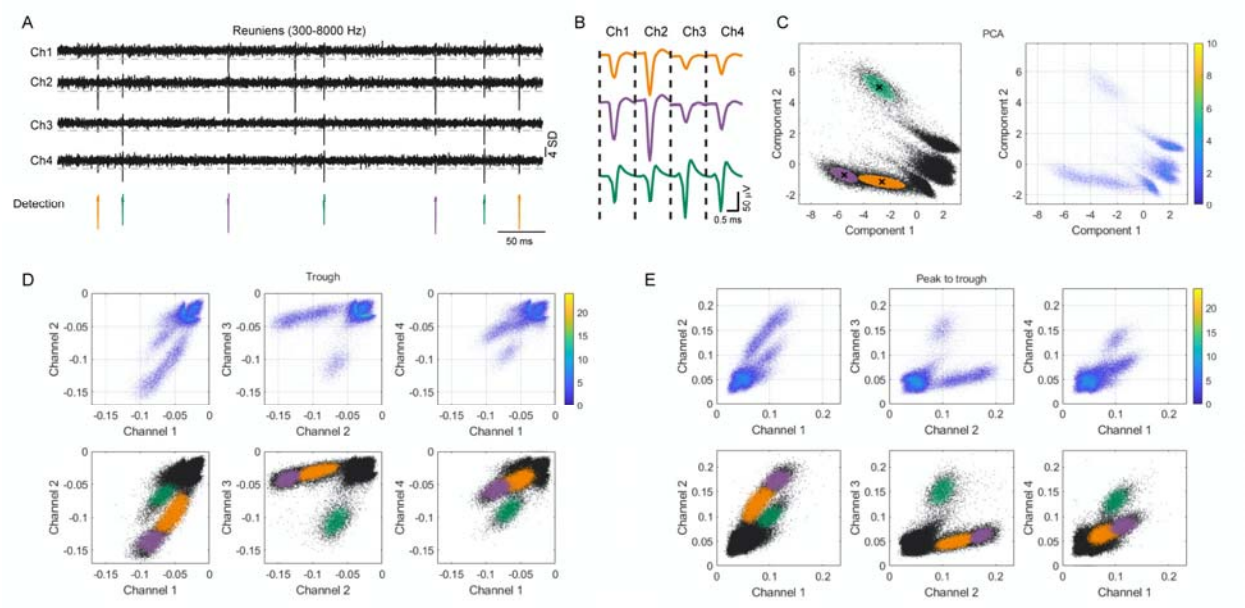

A. Illustrative example of reuniens LFPs with spiking activity, recorded by 4 closely-spaced electrodes in tetrode configuration. Recordings show the bandpass (300-8000 Hz) filtered traces of from 4 channels and detected spikes.

B. Average waveforms of detected spikes, sorted according to clustering of waveform features extracted from the each of the 4 channels.

C. Example of feature clustering for the same recording session as above, showing the principal components 1 versus principal component 2. Clusters were determined by a Gaussian mixture model and further refined by removing spikes with large Mahalanobis distance. Separated clusters indicate three classes of spike waveforms, presumed to have been generated by three distinct neurons (purple, green and pink).

D. Cluster separation for trough values for the same session as above.

E. Cluster separation for the peak-to-trough values for the same session as above.

1281 **Figure 3 – figure supplement 1 Spindle-SWR phase locking**

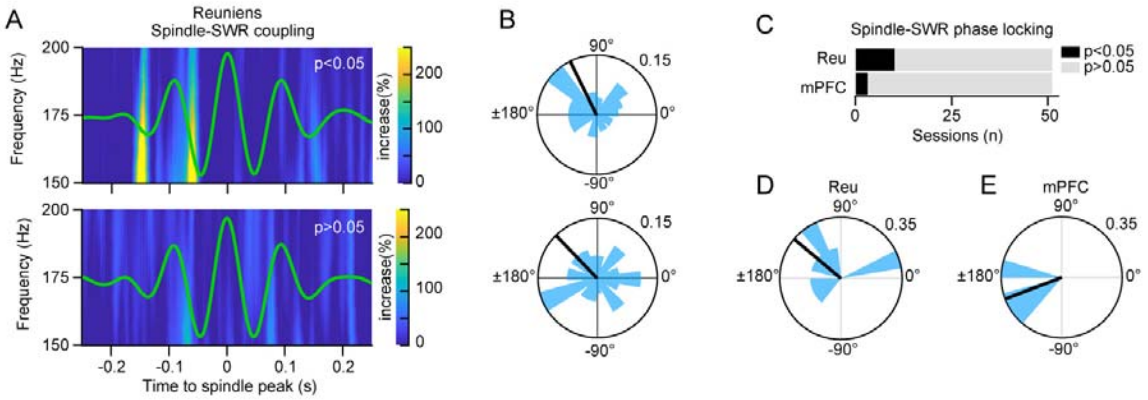

1282

1283 A. Assessment of SWR phase-locking to reuniens spindle cycles for sessions with significant
1284 (top) and not significant (bottom) phase-locking. The TFR shows the average ventral
1285 hippocampal LFP in the ripple band, as percent change from pre-event baseline,
1286 referenced to the peak of the reuniens spindle (time 0) . Green curve shows grand
1287 average of the reuniens LFP, filtered in the spindle frequency range (7-15 Hz).

1288 B. Circular histogram of SI angles of SWR amplitude relative to reuniens spindle phase for
1289 the same two sessions as in A, showing significant (p = 0.009, Rayleigh test) and not
1290 significant phase-locking (p = 0.893, Rayleigh test)

1291 C. Proportion of recording sessions with significant SWR-reuniens spindle coupling phase.

1292 D. Population data of sessions with significant SWR-reuniens spindle coupling phase,
1293 showing the phase histogram of SWR amplitude with respect to spindle cycles and the
1294 mean phase preference (black line, n = 10).

1295 E. The same as D for SWR-mPFC spindle coupling (n = 3).

1296

Table 1 Spindle-SWR coupling, p-values per session.

Recording Session	Recording Duration (s)	Sleep Duration (s)	**mPFC-hipp** p-val.	**Reu-hipp** p-val.
Amande_Day6S2	5888	1460	0.273	0.786
Amande_Day7S1	8210	720	0.726	0.718
Amande_Day7S2	3573	2180	0.74	0.204
Amande_Day8S1	8343	720	0.202	**0.022**
Amande_Day8S2	5734	1900	0.505	0.927
Amande_Day8S3	5693	1420	0.65	0.725
Amande_Day9S1	4543	660	**0.039**	0.875
Amande_Day9S2	4413	1560	0.757	0.866
Amande_Day9S3	4943	3640	0.964	0.066
Amande_Day10S1	3163	240	0.318	0.772
Amande_Day10S2	6488	4560	0.767	0.152
Amande_Day11S1	3033	440	0.068	0.429
Amande_Day11S2	9016	4710	0.594	**0.019**
Cocotte_Day4S1	6763	1900	0.155	0.034
Cocotte_Day4S2	4033	1000	0.081	0.505
Cocotte_Day5S1	6423	1720	0.975	0.427
Cocotte_Day6S1	6043	580	0.72	**0.013**
Cocotte_Day6S2	6033	1780	0.429	0.571

Cocotte_Day7S1	5965	2160	0.494	0.681
Cocotte_Day7S2	4190	1580	0.617	0.78
Cocotte_Day7S3	5495	2700	0.91	0.139
Cocotte_Day8S1	8389	5480	0.449	**6.36E-04**
Cocotte_Day8S2	6578	4700	0.476	**0.019**
Cocotte_Day8S3	2588	720	0.798	0.619
Cocotte_Day9S1	10073	6520	0.937	0.174
Cocotte_Day9S2	5289	2740	0.581	**0.046**
Cocotte_Day10S1	4583	480	0.142	0.957
Cocotte_Day10S2	5953	4100	0.358	0.624
Cocotte_Day10S3	6018	2280	0.667	0.386
Cocotte_Day11S1	14023	9680	0.055	0.104
Cocotte_Day12S1	9863	6840	0.646	0.928
Garfield_Day4S2	3428	940	0.187	0.234
Garfield_Day4S3	4753	1720	**0.003**	0.013
Garfield_Day5S1	8439	1920	0.737	0.345
Garfield_Day5S2	6464	2680	0.123	0.557
Garfield_Day6S1	8073	2080	0.396	0.781
Garfield_Day6S2	7073	4400	0.065	0.895
Garfield_Day7S1	8623	2700	0.619	0.494
Garfield_Day7S2	6664	4360	0.277	**0.002**
Garfield_Day8S1	4884	340	0.775	0.929
Garfield_Day8S2	5468	2520	0.556	0.237

Garfield_Day8S3	4438	3020	0.497	0.319
Garfield_Day9S1	4438	2980	0.3	0.248
Garfield_Day9S2	4568	1780	0.321	0.43
Garfield_Day9S3	6329	3680	**0.029**	**0.013**
Garfield_Day10S1	7068	840	0.719	0.409
Garfield_Day10S2	1089	120	0.459	0.135
Garfield_Day11S1	6684	1980	0.857	0.258
Garfield_Day12S1	5893	1520	0.538	0.971
Garfield_Day12S2	7503	3360	0.633	0.701
Garfield_Day13S1	3063	300	0.296	0.466

Bold indicates significant values.

Article and author information

Author Details

Diellor Basha

Département de psychiatrie et de neurosciences, Université Laval, Québec, QC,Canada

CERVO Centre de recherche, Université Laval, Québec, QC, Canada

Contribution: Conceptualization, Methodology, Investigation, Software, Visualization, Formal Analysis, Data Curation, Writing - Original Draft

Competing interests: No competing interests declared.

Amirmohammad Azarmehri

Department of Electrical Engineering, Ferdowsi University of Mashhad, Mashhad, Iran

Contribution: Methodology, Software, Visualization, Formal Analysis, Writing-Original Draft

Competing interests: No competing interests declared.

Eliane Proulx

Département de psychiatrie et de neurosciences, Université Laval, Québec, QC,Canada

Current address: CNS Diseases Research, Boehringer Ingelheim Pharma GmbH & Co. KG, Biberach an der Riß, Baden-Württemberg, Germany

Contribution: Methodology, Investigation, Visualization, Formal Analysis, Data Curation, Writing – Original Draft

Competing interests: No competing interests declared.

Sylvain Chauvette

CERVO Centre de recherche, Université Laval, Québec, QC, Canada

Contribution: Methodology, Investigation, Validation, Resources, Writing - Review & Editing

Competing interests: No competing interests declared.

Maryam Ghorbani

Department of Electrical Engineering, Ferdowsi University of Mashhad, Mashhad, Iran

Contribution: Conceptualization, Methodology, Investigation, Validation, Writing - Review & Editing, Supervision, Project administration

Competing interests: No competing interests declared.

Igor Timofeev

Département de psychiatrie et de neurosciences, Université Laval, Québec, QC,Canada

CERVO Centre de recherche, Université Laval, Québec, QC, Canada

Contribution: Conceptualization, Methodology, Investigation, Validation, Writing - Review & Editing, Supervision, Project administration, Funding Acquisition.

Competing interests: No competing interests declared.

For correspondence: igor.timofeev@fmed.ulaval.ca

Centre de recherche CERVO, 2601 de la Canardiere Quebec, QC, Canada

Funding

National Sciences and Engineering Research Council of Canada (grant RGPIN-2018-06291)

Igor Timofeev

Canadian Institutes of Health Research (grants PTJ - 183862)

Igor Timofeev

Acknowledgements

We thank Serge Ftomov for technical assistance.